

Multiple Jets from the High-Mass (Proto)stellar Cluster AFGL5142

Qizhou Zhang¹, Todd R. Hunter¹, H. Beuther², T. K. Sridharan¹, S.-Y. Liu³, Y.-N. Su³,
H.-R. Chen³, Y. Chen¹

¹*Harvard Smithsonian Center for Astrophysics
60 Garden Street
Cambridge, Massachusetts 02138, USA*

²*Max-Planck-Institute for Astronomy
Königstuhl 17, 69117 Heidelberg, Germany*

³*Academia Sinica Institute of Astronomy and Astrophysics, P.O. Box 23-141, Taipei 106,
Taiwan*

ABSTRACT

We present studies of a massive protocluster AFGL5142 in the J=2-1 transition of the CO isotopologues, SO, CH₃OH and CH₃CN lines, as well as continuum at 225 GHz and 8.4 GHz. The 225 GHz continuum emission reveals three prominent peaks MM-1, MM-2 and MM-3 with estimated circumstellar material of 3, 3, and 2 M_⊙, respectively. MM-1 and MM-2 are associated with strong CH₃CN emission with temperatures of 90 ± 20 and 250 ± 40 K, respectively, while both MM-1 and MM-3 are associated with faint continuum emission at 8.4 GHz. The heating implied by the temperature indicates that MM-1 and MM-2 cores contain embedded massive young stars. Additional dust continuum peaks MM-4 and MM-5 appear to be associated with H₂O masers. With many continuum sources at cm and mm wavelengths, and those already identified in the infrared, this region is forming a cluster of stars.

A total of 22 lines from 9 molecules are detected. The line strength varies remarkably in the region. The strong SO emission is found both in molecular outflows and cloud cores. CH₃OH emission, on the contrary, is much weaker in molecular outflows, and is detected toward hot cores MM-1 and MM-2 only, but is absent in less massive and perhaps less evolved cores MM-3, MM-4 and MM-5. The modeling of the CH₃CN spectra yields an abundance relative to H₂ of 1×10^{-8} and 4×10^{-8} for the MM-1 and MM-2 cores, respectively. With similar core mass, the higher temperature and CH₃CN abundance in the MM-2 core suggest that it might be at a more evolved stage than the MM-1 core.

The CO and SO emission reveals at least three molecular outflows originating from the center of the dust core. The outflows are well collimated, with terminal velocities up to 50 km s^{-1} from the cloud velocity. Outflow A coincides with the SiO jet identified previously by Hunter et al. (1999). The maximum velocity of both the CO and SiO outflow increases with the distance from the driving source. Since jet-like outflows and disk-mediated accretion process are physically connected, the well collimated outflows indicate that even in this cluster environment, accretion is responsible for the formation of individual stars in the cluster.

Subject headings: ISM: kinematics and dynamics — ISM: H II regions — ISM: clouds — Masers — ISM: individual (AFGL 5142) — stars: formation

1. Introduction

AFGL 5142 is a high-mass star forming region at a distance of 1.8 kpc (Snell et al. 1988). There are two centers of high-mass star formation in this region: IRAS 05274+3345 exhibits bright near infrared (IR) emission (Hunter et al. 1995) with a far IR luminosity of $3 \times 10^3 L_{\odot}$, but has little dense molecular gas associated with it (Estalella et al. 1993). About $30''$ to the east of IRAS 05274+3345 (referred as IRAS 05274+3345 East) lies a faint cm continuum source of about 1 mJy at 3.6cm (Torrelles et al. 1992). If the continuum emission arises from an optically thin, homogeneous HII region, the flux density is equivalent to a zero-age main-sequence (ZAMS) star of spectral type B2 or earlier (Hunter et al. 1995; Torrelles et al. 1992). The source is also associated with emission from dust, dense molecular gas in NH_3 , CS, HCN, HCO^+ , CH_3OH , and CH_3CN (Estalella et al. 1993; Hunter et al. 1995, 1999; Cesaroni et al. 1999; Slysh et al. 1997; Pestalozzi et al. 2005), and H_2O , OH and class II CH_3OH masers (Hunter et al. 1995, 1999; Goddi et al. 2005; Slysh et al. 1997; Pestalozzi et al. 2005). High resolution images reveal a cluster of H_2O masers distributed in an area of $5''$. At a resolution of $3''$, a 3mm continuum core is found with its peak coincident with the cm continuum source (Hunter et al. 1999). All the information indicates that IRAS 05274+3345 is a more evolved region, while the active star formation occurs in the dense core $30''$ to the east.

Hunter et al. (1995) reported two outflows in the CO 2-1 line: An extended remnant flow in the southeast-northwest orientation possibly driven by the brightest near infrared source near IRAS05274+3345, and a compact active outflow in the north-south orientation originating from the cm/dust continuum emission IRAS05274+3345 East. This north-south outflow component is also seen in the CO 3-2 line observed with the CSO (Hunter et al. 1995). Follow up studies at high angular resolution from OVRO revealed a well collimated SiO jet

and an HCO^+ outflow in the north-south orientation (Hunter et al. 1999). In addition, there appears to be a uni-polar outflow in the HCO^+ emission at a 35° position angle. Both outflows appear to originate from the 3mm continuum peak which is unresolved at $3''$ resolution. Copious near infrared H_2 emission knots are associated with the outflow lobes (Hunter et al. 1999; Chen et al. 2005). The high resolution NH_3 studies with the VLA reveal a compact disk-like structure of $1''.2$ in size with large line width of 6.4 km s^{-1} , and a velocity gradient over a scale of 2000 AU (Zhang et al. 2002). This NH_3 structure coincides with the peak of the cm and mm emission, and was interpreted as a rotating disk surrounding a massive star.

However, with a spatial resolution of $3''$, the mm observations from OVRO may not resolve close binaries in a cluster environment. In order to further investigate the outflow, and the structure and kinematics in the core, we observed the IRAS 05274+3345 East region with the Submillimeter Array in CO and its isotopologues, dense gas tracers and 1.3mm continuum emission at a resolution of about $1''$. In addition, we also obtained the 3.6 cm continuum image from the Very Large Array. The continuum images at 1.3mm and 3.6cm indeed reveal multiple emission peaks. The CO and SO emission reveal at least three molecular outflows. In Section 2, we present the observational setup. In Section 3, we describe the main results revealed in the study. And in Section 4, we discuss the findings in the context of cluster formation. We conclude in Section 5 with the main findings of the investigation.

2. Observations and Data Reduction

2.1. SMA

Observations of AFGL5142 were carried out with the Submillimeter Array ¹ (Ho et al. 2004) on 2004 January 11 with six antennas in the compact configuration, and on 2004 February 17 with 8 antennas in the extended configuration. The projected baselines of the two array configurations range from 15m to 210m (11 to 160 $k\lambda$). The double sideband receivers cover 2 GHz band width at IF frequencies of 4 – 6 GHz. The receivers were tuned to the LO frequency of 225 GHz to capture ^{13}CO 2-1, C^{18}O 2-1, and CH_3CN 12-11 in the lower side band, and ^{12}CO 2-1 in the upper side band. The digital correlator was configured to provide a uniform channel spacing of 0.8125 MHz ($\sim 1 \text{ km s}^{-1}$) across the entire band. A

¹The Submillimeter Array is a joint project between the Smithsonian Astrophysical Observatory and the Academia Sinica Institute of Astronomy and Astrophysics, and is funded by the Smithsonian Institution and the Academia Sinica.

detailed description of the SMA is given in Ho et al. (2004).

The primary beam of the SMA at this frequency is about $57''$. The phase center for the observations is $\alpha(J2000) = 05^h30^m48^s.02$, $\delta(J2000) = 33^\circ47'54''.47$. We used quasars 0359+509 and 0555+398 to calibrate time dependent gains, and Jupiter to remove the gain variations across the passband. The flux scale was referenced to the Jovian moon Callisto. The visibility data were calibrated with the IDL superset MIR package² developed for the Owens Valley Interferometer. The absolute flux level is accurate to about 15%. After the calibration in MIR, the visibility data were exported to the MIRIAD format for further processing and imaging. The continuum is constructed from the line free channels in the visibility domain, and is further self-calibrated using the clean components of the image as input models. The gain solution from the self calibration is applied to the spectral line data. The rms in the naturally weighted maps is 4.4 mJy/beam in the continuum, and 90 mJy beam⁻¹ per 1.2 km s⁻¹ channel in the line data. The synthesized beams of the images vary from $1''$ to $3''$ (1700AU to 5100 AU) depending on the weighting of the visibilities in the Fourier transformation. The uncertainty in the absolute position is $\lesssim 0''.2$, derived from comparing quasar positions from two sidebands.

2.2. VLA

Observations of AFGL5142 with the Very Large Array³ were carried out on 2003 June 15 in the A configuration. The correlator was configured in the continuum mode at 3.6cm with a total bandwidth of 200 MHz. The visibility data were made available to public through the VLA data archive. The pointing center is the same as that of the SMA. The primary beam of the VLA is about $6'$ at this frequency. 3C147 was used as the flux calibrator, and 0443+346 was used as the gain calibrator. The visibility data were calibrated using the AIPS package. The rms in the naturally weighted image is 0.09 mJy beam⁻¹, with a synthesized beam of $0''.32 \times 0''.26$ (or 510×440 AU) at a position angle of $58^\circ.6$. The uncertainty in the absolute position is better than $0''.03$, one-tenth of the synthesized beam.

²<http://www.cfa.harvard.edu/~cqi/mircook.html>

³The National Radio Astronomy Observatory is operated by Associated Universities, Inc., under cooperative agreement with the National Science Foundation.

2.3. Supplemental Short Spacing Information to the ^{12}CO Emission

The shortest projected baseline ($11k\lambda$) in the SMA observations corresponds to a spatial scale of $1.2\frac{\lambda}{b}$, or $20''$. Here b is the length of the projected baseline. Spatial structures more extended than $20''$ were not sampled in the SMA observations. This filtering effect can affect the appearance of images of easily excited molecular lines such as CO. To recover the missing short spacing information in the ^{12}CO 2-1 line, we add the single dish data obtained from the CSO (Hunter et al. 1995) to the SMA data, following a procedure outlined in Zhang et al. (1995). The CSO spectra have a velocity range from -35 to 30 km s^{-1} , and do not cover the entire high velocity wings detected in the SMA data. However, the highest velocity CO emission appears to be spatially compact, thus does not suffer strongly the missing flux problem.

The combined image of the ^{12}CO 2-1 line, when convolved to the $29''$ beam of the CSO, recovers about 90% of the flux from the single dish telescope. The ^{13}CO 2-1 emission from the SMA also appears to miss extended emission around the cloud systemic velocity. For that reason, we will avoid interpreting the ^{13}CO image around the cloud systemic velocity.

3. Results

3.1. Continuum Emission

Figure 1 presents the continuum images at 225 GHz (1.3 mm) and 8.4 GHz (3.6 cm) overlaid with the H_2O maser emission from Hunter et al. (1999). The VLA image reveals three continuum peaks. The two peaks, CM-1A and CM-1B in the north are separated by $0.2''$. They have a peak intensity of 0.65 mJy/beam and 0.64 mJy/beam, respectively, well detected above the 1σ rms of 0.09 mJy/beam. These two peaks were not resolved in previous observations with the VLA. The integrated flux of the two sources are 1.4 mJy, consistent with observations at lower resolution (Hunter et al. 1999). There appears to be an additional cm continuum source $2''$ to the south of CM-1A/1B. This source, labeled as CM-2, has a flux intensity of 0.35 mJy/beam. CM-2 was not reported in the previous observations possibly due to confusion from the extended emission.

At a resolution of $1''.3 \times 0''.8$, the 225GHz continuum image reveals two dominant peaks separated by about $1''$. The northern peak, MM-1, coincides with two 8.4 GHz continuum peaks CM-1A/1B. The southern peak, MM-2, does not have any counterpart at 8.4 GHz at a 1σ sensitivity of 0.09 mJy/beam.

In addition to MM-1 and MM-2, there exist other mm continuum peaks. The extension

toward the southwest from MM-2, labeled as MM-3, is close to the the cm emission feature CM-2. The H₂O maser feature 3'' to the east of MM-1 coincides with a dust peak MM-4. Furthermore, a dust emission peak lies about 2'' west of MM-3. We refer to this peak as MM-5. The flux density per beam at the continuum peaks are listed in Table 1. The expected contribution from the ionized gas at mm and submm wavelengths is $\lesssim 1$ mJy (Hunter et al. 1999). Thus, dust emission dominates the 1.3mm continuum flux of all the sources, and likely does so to wavelengths as long as ~ 3 mm. Because of a lack of high resolution images at more than one wavelength, the emissivity index of the dust emission at each peak cannot be evaluated. Instead, we convolve the continuum map at 225 GHz to the same synthesized beam as the 88 GHz map in Hunter et al. (1999) to estimate an average emissivity index for the region. We obtain a peak flux density of 0.62 Jy at 225 GHz. Comparing with the flux density of 0.038 Jy measured in the same beam at 88 GHz, we derived an index $\alpha = 3$, or an emissivity index of $\beta = 1$. This β is smaller than the typical value of 2 for the interstellar dust, but is consistent with the value in a similar object IRAS 20126+4104 (Cesaroni et al. 1999). Using the Hildebrand dust opacity law (Hildebrand 1983), we find the dust opacity per unit dust mass $\kappa_0(225GHz) = 1.8 \text{ cm}^{-2}/\text{g}$. For a dust temperature of 45 K based on the estimate in Hunter et al. (1999), and an integrated flux of 1.5 Jy, we obtain a total mass of $50 M_\odot$ in the region. We note that this mass is smaller than $145 M_\odot$ derived from the 3mm flux in Hunter et al. (1999). The difference is attributed mostly to the dust opacity: Hunter et al. (1999) adopted an opacity of $0.5 \text{ cm}^{-2}/\text{g}$ at 230 GHz, which is about 30% of the opacity used in this paper, and hence resulted in a higher mass estimate. With the Hildebrand dust opacity, the circumstellar mass within one synthesized beam ($\sim 1800\text{AU}$) estimated from the 225 GHz peak flux is $3 M_\odot$ for MM-1 and MM-2, respectively. The kinetic temperature toward MM-3, MM-4 and MM-5 is about 20 K based on the NH₃ studies (Zhang et al. 2002). At that temperature, we derive a mass of $2 M_\odot$ for MM-3, $0.9 M_\odot$ for MM-4, and $0.7 M_\odot$ for MM-5, respectively.

As shown in Figure 1, MM-1 appears to coincide with CM-1A/1B, and MM-3 appears to coincide with CM-2. The maximum offset among the cm/mm counterparts is $< 0''.2$, within the uncertainty in the astrometry of the SMA image. Therefore, the spatial displacement between the mm and cm peaks may not be physical. The centimeter emission likely arises either from the HII region due to ionization of massive stars or from the ionized wind emission in outflows. In general, the thermal free-free emission from the HII region tends to have a negative spectral index α (defined as $F_\nu \propto \nu^\alpha$) of about -0.1 in the optically thin limit. On the other hand, the emission from the ionized wind tends to have a positive spectral index of about 0.6 (Anglada et al. 1998). Without images of similar resolution at other cm wavelengths, we cannot access the physical nature of the emission. If the emission arises from the optically thin and homogeneous ionized gas in the HII region, the flux density from the

three cm peaks corresponds to ZAMS stars of spectral type B3 to B2. However, as discussed in Section 4.1, the 3.6cm emission is probably due to ionized wind emission from outflows.

3.2. Line Emission

3.2.1. Line Spectroscopy

Figure 2 shows the SMA spectra in the lower side band and the upper side band toward the position of MM-1, MM-2, MM-3 and the red-shifted peak of the outflow A (marked as the triangle in Figure 3). The data are subtracted by the continuum emission constructed from the line-free channels in the visibility domain, and then imaged with robust weighting, resulting in a synthesized beam of $1''.3 \times 0''.8$ at a position angle of -60° . Thus, the spectra taken from the three dust continuum peaks are spatially resolved from each other. In order to increase S/N, the spectrum toward the outflow A is made with the natural weighting and a spatial tapering of $3''$, resulting in a resolution of $4''.3 \times 3''.6$ at a position angle of -80° .

Similar to other massive star forming regions (Beuther et al. 2004a,b), multiple molecular lines are detected in the AFGL 5142 region. We detect 22 spectral lines/components from ^{12}CO , ^{13}CO , C^{18}O , CH_3CN , CH_3OH , SO , HNCO , OCS and H_2^{13}CO molecules (see Table 2). The energy levels of the lines range from 17 K for CO to 579 K for CH_3OH with critical densities from 10^2 cm^{-3} to 10^7 cm^{-3} . These lines sample a wide range of physical and chemical conditions in the region. The peak in the ^{12}CO 2-1 line appears to be weaker than that of the ^{13}CO . This is likely due to high optical depths near the cloud LSR velocity and extended emission missed by the interferometer.

As shown in Figure 2, the strength of the molecular lines varies significantly in this region. ^{12}CO and SO are the only molecular lines detected toward all four positions. MM-1 and MM-2 appear to emit in nearly all the molecular lines identified in the region, including hot core molecules CH_3CN and CH_3OH . MM-3, a faint cm source with a mass similar to that of MM-1 and MM-2, is not detected in any of these hot core molecules. This suggests that MM-3 core has a lower gas temperature than in the MM-2 and MM-1 cores. The presence of SO toward the outflow indicates that the SO abundance is enhanced greatly in the outflow as compared to the core.

Table 2 lists the flux and linewidth of the molecular lines detected toward MM-1 and MM-2.

3.2.2. Line Emission from the Core

Figure 3 shows the images of the velocity integrated flux from ^{13}CO J=2-1, C^{18}O J=2-1, $\text{SO } 6_5 - 5_4$, $\text{CH}_3\text{OH } 8_{-1,8} - 7_{0,7}$ E at 229.759 GHz, OCS J=19-18, and $\text{HNCO } 10_{0,10} - 9_{0,9}$ at 219.798 GHz. Emission from all the molecules presented here is seen toward the core surrounding MM-1 and MM2. The ^{13}CO emission around the cloud velocity appears to be extended and likely suffers from missing large scale component. Thus, we will not discuss the emission in details. The SO emission reveals an extended component corresponding to molecular outflows and we will interpret the data in Section 3.2.3. The emission from OCS and HNCO is associated with dense cores surrounding MM-1 and MM2 only, and shows the most compact structure. The CH_3OH emission likely arises from both dense core and outflow.

The CH_3CN J=12-11 line also displays compact emission similar to that of OCS and HNCO . Figure 4 presents the integrated CH_3CN emission and the spectra toward MM-1 and MM-2. At a resolution of $1''.3 \times 0''.8$, the two mm continuum sources are resolved from each other in the CH_3CN emission. As shown in the CH_3CN spectra, the emission from MM-2 is much stronger than that from MM-1, thus dominates the integrated flux in Figure 4. The hyperfine components of the $K=0$ to 6 of CH_3CN with energy levels from 69 to 326 K are detected. The emission from the higher K components of CH_3CN toward MM-1 is much weaker than that toward MM-2. This indicates that MM-1 has a lower temperature than MM-2. Despite the difference in statistical weights by a factor of 2, the $K=2$ and 3 components from both sources have similar brightness temperatures, indicating a moderate optical depth in the lines. Assuming LTE, we fit the CH_3CN line profiles using a radiative transfer model in a uniform, isothermal spherical core (Chen et al. 2006). The emergent spectrum depends on the gas temperature, density, central velocity, linewidth and the size of the emitting region. By varying these parameters, we obtain the best fit by minimizing the χ^2 between the observed and model spectra. This approach takes into account the optical depth effect, thus, produces a better fit to the line profiles of all the K components than using the energy diagram which assumes optically thin emission (e.g. (Zhang et al. 1998)). Figure 4 shows the CH_3CN J=12-11 lines reproduced from the model: The match between the observed and model spectra is reasonable. The fitting yields $V_{\text{LSR}} = -1 \pm 0.2 \text{ km s}^{-1}$, $\text{FWHM} = 4.7 \pm 0.5 \text{ km s}^{-1}$, $T_K = 90 \pm 20 \text{ K}$, $n_{\text{CH}_3\text{CN}} = 1.3 \pm 0.7 \text{ cm}^{-3}$ and the core radius $R = 440 \pm 80 \text{ AU}$ for MM-1, and $V_{\text{LSR}} = -3.4 \pm 0.1 \text{ km s}^{-1}$, $\text{FWHM} = 4.0 \pm 0.2 \text{ km s}^{-1}$, $T_K = 250 \pm 40 \text{ K}$, $n_{\text{CH}_3\text{CN}} = 6 \pm 4 \text{ cm}^{-3}$ and $R = 380 \pm 80 \text{ AU}$ for MM-2. The central velocity of the CH_3CN cores toward MM-1 and MM-2 differs by 2.4 km s^{-1} . This difference, also seen in the SO and CH_3OH emission, confirms that both dust continuum sources contribute to the observed CH_3CN emission.

The temperature and density derived from CH₃CN reveal that the physical conditions in the MM-1 and MM-2 cores are different. MM-2 has much higher temperature and column density than MM-1. As shown in Table 2 and Figures 2 and 4, the higher K components of the CH₃CN line toward MM-1 are weaker than toward MM-2. In addition, emission from higher energy levels of CH₃OH and HNCO are much weaker or not detected toward MM-1. These measurements are consistent with a lower temperature and a lower CH₃CN density toward MM-1. From the dust emission, MM-1 and MM-2 have a similar peak flux. At the assumed dust temperature of 45 K, the mass in both cores (3 M_⊙) yields a mean H₂ density of $1.5 \times 10^8 \text{ cm}^{-3}$ averaged over the volume of the synthesized beam (1800AU). Thus, the fractional abundance of CH₃CN relative to H₂ is 1×10^{-8} and 4×10^{-8} toward MM-1 and MM-2, respectively. Both values are two orders of magnitude higher than the abundance in dark clouds (Herbst & Leung 1990), similar to that in the hot core (Wilner et al. 1994). The abundance in the MM-2 is higher than in the MM-1 core. Based on the fitting of the CH₃CN spectra, MM-2 has a gas temperature 2.5 times of that in the MM-1 core. If the gas and dust reach an equilibrium temperature, the mass and hence the average H₂ density in MM-2 should be smaller than in MM-1. This would result in even higher CH₃CN abundance toward MM-2. The higher CH₃CN abundance in MM-2 is likely the result of higher temperature in the MM-2 core, which enhances the production of CH₃CN.

In addition to CH₃CN, emissions from SO, OCS, HNCO and CO isotopologues are also detected toward MM-1 and MM-2. The central velocity of the emission from these molecular lines is centered around -1 and -3.4 km s⁻¹ for MM-1 and MM-2, similar to the that in the CH₃CN emission. As shown in Section 3.2.3, the SO and CH₃OH emission can arise from outflows. The agreement of the line velocity indicates that the SO and CH₃OH emission toward MM-1 and MM-2 arise from the dense core.

Unlike MM-1 and MM-2, far fewer molecular lines are detected toward MM-3. In particular, CH₃CN, CH₃OH, OCS and HNCO are all absent (at a 1σ sensitivity of 0.09 Jy), despite the presence of faint 8.4 GHz emission. The absence of these lines also indicates that MM-3 is at a lower temperature than that of the MM-1 and MM-2 cores.

3.2.3. *Molecular Outflows*

Figure 5 presents the channel maps of the ¹²CO 2-1 line. Since the single dish CO 2-1 data from the CSO do not cover the high velocity wing emission, the combined SMA and CSO data have a limited velocity coverage from -35 to 30 km s⁻¹. The CO emission at $\Delta V > 15 \text{ km s}^{-1}$ is compact and subjects to little missing flux. Thus, we show in Figure 5a the high velocity emission obtained from the SMA alone. Figure 5b presents the low

velocity CO emission from the combined SMA and CSO data. From the CO emission, one can immediately identify an outflow in the north-south direction. The CO 2-1 emission from the CSO (Hunter et al. 1995) peaks at -3.9 km s^{-1} . At the red-shifted velocities of 10 to 48 km s^{-1} , there exists high velocity gas toward the north of the mm continuum peaks at a position angle of 5° . The well-collimated CO emission is detected up to 50 km s^{-1} from the cloud systematic velocity and extends up to $30''$ from the mm continuum sources. The velocity of the red-shifted CO emission increases with the distance from the mm continuum sources. The red-shifted lobe appears to be clumpy. The peak of the CO clumps is not aligned along the outflow axis and spans an angle of $\sim 5^\circ$ with respect to the dust continuum peaks (see channels from 12 to 45 km s^{-1} in Figure 5a). The blue-shifted side of the outflow extends about $5''$ to the south from the mm continuum peaks, with the CO emission detected up to -13 km s^{-1} . This outflow, referred as outflow A, coincides spatially with the high velocity SiO outflow reported in Hunter et al. (1999).

Additional high velocity CO emission suggests the presence of other outflows. At the blue-shifted velocities of -14 to -26 km s^{-1} , the CO emission at a position angle of 35° identifies the outflow B. The lobe to the southwest of the mm continuum sources is mainly blue-shifted with CO emission detected up to -22 km s^{-1} from the cloud velocity. The lobe to the northeast exhibits both blue- and red-shifted emission from -18 to 15 km s^{-1} . Weak CO emission is detected about $30''$ southwest of the mm continuum peaks. The possible third outflow, outflow C, originates from the mm core at a position angle of -60° . The lobe to the northwest of the mm continuum peaks has a bifurcated structure at -8 km s^{-1} , extending $20''$ to the northwest. Higher velocity emission of $\pm 25 \text{ km s}^{-1}$ is seen toward one side of the shell. The lobe to the southeast has a lower velocity with a jet like feature seen in the -8 km s^{-1} channel.

Furthermore, there appear to be additional high velocity features that may arise from other outflows. For example, the CO emission around $[-15'', -15'']$ from MM-2 seen at velocity channels of -16.8 and -10.4 km s^{-1} does not align with any of the three outflows identified and may trace a fourth outflow in the region.

Figure 6 presents the position velocity plots of the three outflows identified above. To show the full velocity extent of the outflows, we use the image from the SMA data only. The negative contours (dotted lines in Figure 6) near the cloud velocity arise from the effect of missing short spacing flux. Figure 6 reveals that the maximum velocity in the outflow A increases with the distance from the driving source. This ‘Hubble’-law relation has been seen in molecular outflows toward both high- and low-mass stars (Su et al. 2004; Lada & Fich 1996; Gueth & Guilloteau 1999). Outflows B and C show rather complex velocity structures, with both the blue- and red-shifted high velocity gas toward the same side of the lobes. This

may indicate additional outflows in the region.

Figure 7 shows the channel maps of the SO 6_5-5_4 transition. SO is present in dark clouds (Swade 1989), and its abundance is enhanced in outflows (Bachiller et al. 2001; Viti et al. 2003). The process involves the photo evaporation of sulphur bearing molecules such as H_2S from dust grains near shocks. The gas phase H_2S then reacts with OH and O_2 to produce SO and SO_2 . Strong SO emission is detected toward the CO outflows in AFGL5142, but at velocities much closer to the cloud velocity: The SO emission is detected within a velocity range of -15 to 8 km s^{-1} , while the CO emission is seen between -26 and 50 km s^{-1} . Despite the velocity difference from the CO emission, SO emission appears in all three molecular outflows. Outflow A is seen in both the red-shifted (-3.8 to 5.8 km s^{-1}) and blue-shifted emission (-3.8 to -7.4 km s^{-1}). The spatial extent of the blue-shifted and the red-shifted lobes is similar to that of the CO outflow. The outflow B is clearly seen in SO as well: The red-shifted emission in the northeast is detected from -8.6 to 5.8 km s^{-1} , while the blue-shifted emission to the southwest is from -3.8 to -12.2 km s^{-1} . For outflow C, the SO emission is mostly seen from 2.2 to -8.6 km s^{-1} for the lobe in the southeast, and 5.8 to -2.6 km s^{-1} for the lobe in the northwest.

In addition to SO, the CH_3OH emission is detected in the outflows as well. Although CH_3OH abundance is low ($< 10^{-9}$) in dark clouds, UV radiation from outflow shocks can release CH_3OH from dust grains, and enhance the CH_3OH abundance in molecular outflows (Bachiller et al. 2001; Viti & Williams 1999). Figure 8 presents the channel maps of the CH_3OH transition $8_{-1,8} - 7_{1,6} \text{ E}$. The strongest emission is detected along outflow B at velocity channels from -0.2 to -7.4 km s^{-1} . In addition, an extension to the northwest from MM-1, MM-2 and MM-3 appears to be associated with outflow C. In general, the CH_3OH emission in the outflow is much weaker than the SO emission and appears at lower velocities than CO and SO. Furthermore, the CH_3OH emission does not always coincide with the SO emission spatially.

From the CO emission, we estimate the mass and momentum in the outflows. Many studies of molecular outflows assumed optically thin CO emission when estimating outflow parameters. In some cases, an average value of 10 for the ^{12}CO to ^{13}CO ratio is assumed to correct for the optical depth effect (Choi et al. 1993). However, the opacity is in general a function of velocity. As shown in Su et al. (2004), the CO can be optically thick even at high velocity wings. The simultaneous observations of the ^{12}CO and ^{13}CO with the SMA allow us to investigate the CO optical depth in the outflow. Although ^{13}CO suffers missing flux near the cloud velocity, the channel images suggest that such an effect is negligible for emission with $\Delta V > 4 \text{ km s}^{-1}$. By examining the emission ratios, we found that the CO optical depth varies from 4 to 15 in the line wings 5 to 12 km s^{-1} from the cloud velocity.

Making appropriate corrections for the opacity, we find a total mass, momentum and energy of $5.9 M_{\odot}$, $38 M_{\odot} \text{ km s}^{-1}$, and 3.4×10^{45} ergs, respectively, for the red-shifted CO emission from 1.6 to 50 km s^{-1} . Similarly, we integrate the blue-shifted CO emission from -8 to -40 km s^{-1} , and find a mass, momentum and energy in the outflow of $5.7 M_{\odot}$, $32 M_{\odot} \text{ km s}^{-1}$, and 2.5×10^{45} ergs, respectively. There are about equal amounts of mass in the three outflows: 2.5, 3 and $3 M_{\odot}$ in the outflows A, B and C, respectively. The momentum in the outflows are from 12 to $20 M_{\odot} \text{ km s}^{-1}$. The dynamic time scales of the outflows, computed from $\frac{l}{V_{max}}$ are about 10^4 yrs. Here l and V_{max} are the maximum length and velocity of the outflow where the CO emission is detectable at an rms of 0.09 Jy. The outflow parameters for the three outflows are listed in Table 2. Due to the existence of additional high velocity features, the masses from the three outflows do not add up to the total outflow mass for the entire region.

4. Discussions

4.1. Nature of the Continuum Sources

The presence of multiple continuum peaks and a group of H₂O masers indicates a deeply embedded cluster in formation. Both MM-1 and MM-2 give rise to CH₃CN emission with rotational temperatures of 90 and 250K, respectively. Although nearby low-mass protostars may excite hot-core type molecular emission (Ceccarelli et al. 2000; Kuan et al. 2004; Chandler et al. 2005), the emission may not be detectable at larger distances. The protostars that produce heating toward MM-1 and MM-2 and the CH₃CN emission are likely to be massive. Scoville & Kwan (1976) derived a relation between the dust temperature and the luminosity of the star:

$$T_D = 65 \left(\frac{0.1 pc}{r} \right)^{2/(4+\beta)} \left(\frac{L_{star}}{10^5 L_{\odot}} \right)^{1/(1+\beta)} \left(\frac{0.1}{f} \right)^{1/(4+\beta)} K.$$

Here β is the power law index of the dust emissivity at the far infrared wavelengths, $f = 0.08 \text{ cm}^2 \text{ g}^{-1}$ is the value of the dust emissivity at $50 \mu\text{m}$, and r the distance from the star. The dust temperature derived from the fitting to the SED using a grey body assumption gives a dust temperature of 45 K (Hunter et al. 1999). This value corresponds to the average temperature over $> 20''$ scales. At scales of $1''$, dust temperatures probably reach as high as 250K, the gas temperature derived from the CH₃CN emission, if the gas and dust reach thermal equilibrium in the high density environment. With $T_D = 45 - 200 \text{ K}$, $r = 900 \text{ AU}$ the size of dust emission, and $\beta = 1$, we estimate the luminosity of the star of 4×10^3 to $7 \times 10^4 L_{\odot}$. Thus, both protostars are likely to be massive based on their luminosity. MM-2, with higher temperature and CH₃CN abundance may be more evolved than the source embedded in the MM-1 core.

The central velocity of the molecular gas in the two hot cores is offset by 2.4 km s^{-1} . If MM-1 and MM-2 are in a binary, the binding mass of the system is $10/\sin(i) M_{\odot}$, with i being the inclination angle of the orbit. The mass in both cores adds up to $6 M_{\odot}$. If the two protostars are early B type as suggested by the presence of hot cores, the combined stellar mass can be up to $20 M_{\odot}$. Therefore, the total mass in the stars and circumstellar material is large enough to host the binary. If so, the projected separation of the two stars is 1700 AU with an orbital period of about 10^4 yrs.

Dynamical interactions between members in a proto binary system can cause outflow precession. The CO peaks toward the red-shifted lobe of Outflow A exhibit misalignment along the outflow axis, consistent with a precessing jet. Jet precession has been reported in protostellar outflows associated with both low- and high-mass young stars (Zhang et al. 2000; Shepherd et al. 2000). It appears that the precession of 5° in the outflow A is much smaller than the $20^{\circ} - 45^{\circ}$ reported in some of the other protostellar systems such as IRAS 20126+4104 (Shepherd et al. 2000; Lebrón et al. 2006).

MM-3 appears to be associated with the 8.4 GHz emission, but does not have detectable organic molecules indicative of a hot core. If the 8.4 GHz emission arises from the UCHII region, the central star that photoionizes the circumstellar material should also give rise to high temperatures in the molecular gas. The absence of a hot core toward MM-3 indicates a relatively lower temperature in the molecular gas. This fact leads us to suggest that the faint 8.4 GHz emission likely arises from the ionized wind emission driven by an intermediate to high mass protostar in the MM-3 core. Although the ionized wind emission has been detected toward nearby low-mass young stars, the typical flux is on the order of 0.1 to a few mJy (Anglada et al. 1998). Such flux levels, after being scaled down by a factor of 10 to 100 to account for the distance, would not be detectable at the distance of AFGL5142 at an rms of 0.09 mJy/beam. Thus, the ionized wind emission toward MM-3 is likely to be powered by a more massive young star. In a model in which the ionized emission arises from the plane parallel shock when the neutral wind plows into the high density material, Curiel et al. (1989) derived a relation between the momentum rate in the outflow and radio flux:

$$\left(\frac{\dot{P}}{M_{\odot}\text{yr}^{-1}\text{km s}^{-1}}\right) = \frac{10^{-3.5}}{\eta} \left(\frac{S_{\nu}}{\text{mJy}}\right) \left(\frac{d}{\text{kpc}}\right)^2.$$

Here \dot{P} is the momentum rate in the outflow, $\eta = 0.1$ is the efficiency factor corresponding to the fraction of the stellar wind that is shocked and produces the radio emission. For a flux S_{ν} of 0.35 mJy, we obtain an outflow momentum rate $\dot{P} = 4 \times 10^{-3} M_{\odot}\text{yr}^{-1} \text{ km s}^{-1}$. This is in rough agreement with the outflow momentum rate in the CO outflow. In order to test our hypothesis on the ionized wind nature of CM-2, more sensitive cm continuum observations are needed to measure its spectral index.

Additional evidence that MM-3 is powered by an embedded massive star comes from the amount of circumstellar mass present. Although the total mass in MM-3 appears to be smaller as compared to MM-1 and MM-2, the mass estimates from the dust emission depend ($1/T$) on the dust temperature assumed. We assumed a dust temperature of 45 K for MM-1 and MM-2. If we use the gas temperature of 250 K for MM-2, the mass in MM-2 would be $0.7 M_{\odot}$, comparable to the mass in MM-3. Thus, many lines of evidence suggest that MM-3 is an intermediate to massive star at an earlier evolutionary stage than MM-1 and MM-2. At such a stage, the radiation of the central star may not yet have produced a large enough core with high temperature that renders detection in hot core molecules.

In addition to the strong dust peaks MM-1, MM-2 and MM-3, MM-4 coincides with the H_2O maser feature $3''$ to the east of the strong mm peaks. H_2O masers can be excited in dense envelopes ($\sim 10^8 \text{ cm}^{-3}$) surrounding protostars in the interaction with molecular outflows (Elitzur et al. 1989; Felli et al. 1992). Thus, the H_2O maser emission may indicate the presence of a fourth young star.

In contrast to the spatial agreement of a water maser with MM-4, a pair of H_2O masers lie near symmetrically $2''$ to the southeast and northwest of MM-5. There appears to be a high velocity CO feature (see the channel maps at velocities from 4 to 8.8 km s^{-1} in Figure 5b) aligned with this source. This CO feature can be part of outflow C associated with MM1. On the other hand, it could also be a separate outflow associated with MM-5.

4.2. Kinematics and Driving Source of Outflows

Of the three molecular outflows identified in the CO and SO emission, outflow A coincides with a jet-like SiO outflow reported by Hunter et al. (1999). Figure 9 presents an overlay of the position-velocity diagram of the CO and the SiO emission along the axis of the outflow A. For the SiO 2-1 line, strong emission appears around $\pm 6 \text{ km s}^{-1}$ from the cloud systemic velocity. Higher velocity emission is detected up to $\pm 40 \text{ km s}^{-1}$ from the cloud velocity near the position of the driving source, *i.e.*, the position offset around $0''$. The maximum velocities of the SiO emission along the outflow axis increases with the distance from the driving source, similar to that of the CO outflow.

Outflowing gas moving faster than the sound speed in a cloud (a few km s^{-1}) produces shocks when interacting with the core material and enhances the gas temperature. As reported in Zhang et al. (2002), gas heating due to the outflow A is seen in AFGL5142. We re-examined the ratio of the NH_3 (J,K)=(3,3) and (4,4) to the (1,1) line presented in Zhang et al. (2002). Figure 10 shows the NH_3 ratio maps with all three outflows marked.

The NH_3 (J,K) = (1,1), (3,3) and (4,4) emission are from energy levels of 23, 125 and 230 K, respectively. Since upper (J,K) transitions arise from higher energy levels, the higher (3,3)/(1,1) and (4,4)/(1,1) ratios reveal warmer molecular gas. It is clear that in addition to the temperature enhancement along the outflow A, there appears to be enhanced temperatures along outflows B and C.

All three outflows appear to originate from the central core of about $3''$ area. Therefore, it is difficult to identify the driving source. Using the data in this paper, and the H_2O maser distribution and proper motion, we attempt to assign driving sources for the three outflows with a caveat that the assignment may not be unique. There are three cm continuum peaks within the $3''$ region. CM-1A and CM-1B are separated by less than $0''.2$ and coincide with the 225 GHz continuum peak MM-1. The H_2O maser studies with the VLBA by Goddi et al. (2005) show a cluster of masers associated with the CM-1A/1B and MM-1. The masers are concentrated to the northwest and southeast of the continuum source and exhibit proper motion along the axis of $\text{PA}=-40^\circ$. This orientation is close to the axis of the outflow C. Therefore, it is likely that MM-1 is the driving source of the outflow C. The two cm continuum peaks toward MM-1 can be a close binary with a projected separation of 400 AU. On the other hand, CM-1A and CM-1B are aligned in a similar direction as the H_2O maser proper motion. It is more likely that the two centimeter peaks trace an ionized jet in the outflow.

For the outflow B, both the CO and SO lobes (see the channel at -12.8 km s^{-1} in CO) appear to put the MM-3 close to the geometric center. The H_2O maser study by Goddi et al. (2005) also detected a pair of the maser spots at a similar position angle. However, the geometric center of the H_2O masers appears to be north of MM-3, and closer to MM-2. This pair of masers was not detected in other VLA observations (Hunter et al. 1999), thus, their proper motion may be questionable. We propose that MM-3 is the driving source of outflow B.

H_2O masers are also detected in the vicinity ($< 0''.5$) of MM-2. This source, not detected at 8.4 GHz with the VLA at an rms of 0.09 mJy/beam, is associated with a hot core with strong CH_3CN emission. Being the only dominant continuum source remaining, MM-2 probably drives the north-south outflow A.

4.3. Chemical Variations

The AFGL5142 region reveals interesting variations in molecular line emission. SO emission is seen toward cores MM-1, MM-2 and MM-3, while CH_3OH , CH_3CN , OCS and HNC emission are detected only toward two hot cores MM-1 and MM-2. This difference

indicates that SO is abundant during a long period of core evolution from an early and relatively cold stage through a more evolved and warm/hot stage. On the other hand, CH₃OH and CH₃CN are abundant only when massive cores are more evolved such that heating from the central protostar evaporates the molecules from the dust.

SO and CH₃OH emission are also detected toward molecular outflows away from the dense core. This is expected as their abundances are enhanced in outflow shocks where heating and UV radiation from shocks release CH₃OH and sulphur bearing molecules from dust, and enhance the formation of SO in the gas phase. The time scale of the abundance enhancement is 10⁴ yrs (Viti & Williams 1999), consistent with the dynamical time scale of the outflow.

4.4. Cluster Star Formation

The multiple cm/mm continuum sources identified in the AFGL 5142 region indicate a dense cluster in formation. The infrared imaging in J, H and K by Hunter et al. (1995) reveal 30 point sources with IR excess over an area of 3'. However, nearly all the IR sources lie outside of the dense core. The density of the IR sources within the 0.1 pc radius from the mm continuum sources is about 10³ stars pc⁻³. This is much smaller than the average stellar density of $\lesssim 10^5$ pc⁻³ within the central 0.2 pc in Orion Nebula, with 3 O stars within 0.1 pc (Hillenbrand 1997; Hillenbrand & Hartmann 1998). W3 IRS5, a cluster with a total luminosity of $2 \times 10^5 L_{\odot}$, has 5 near IR sources within 5600 AU, equivalent to 6×10^5 stars pc⁻³. Toward AFGL 5142, 3 protostars are revealed in the mm observations with a projected separation of 2''.3, or 4100 AU, which is equivalent to a stellar density of 2×10^5 stars pc⁻³. Because the average is performed over a very small region, this high stellar density is not necessary representative of the entire region. Nevertheless, the AFGL 5142 region appears to form a dense cluster. The luminosity for AFGL5142 is 1-2 orders of magnitude smaller than that of the Orion Nebula and W5 IRS5, and appears to harbor only early B stars. Unlike the Orion Nebula and W3 IRS 5, however, all three protostellar objects in AFGL 5142 appear to be actively accreting because of the presence of outflow activity. It is possible that they may become O stars when the star formation is complete.

Zhang et al. (2002) reported a velocity gradient and large NH₃ linewidth of 6.4 km s⁻¹ toward the peak of the 3mm continuum detected by Hunter et al. (1999). The kinematics in NH₃ appears to be consistent with a rotating disk in the region. Higher resolution observations with the SMA resolved the 3mm dust peak into two sources separated by 1'', which excite two hot cores detected in the CH₃CN emission. The two hot cores have systemic velocities of -1 and -3.4 km s⁻¹, which creates the velocity gradient seen in the NH₃ emission

at lower resolution. Re-examining the data in Zhang et al. (2002), we found that at $\sim 1''$ resolution the NH_3 (3,3) emission shows an elongation in the north-south direction. There appears to be two velocity components in the NH_3 (3,3) channel maps (Figure 2c in Zhang et al. 2002), consistent with the CH_3CN data. Refitting the $1''$ resolution NH_3 (3,3) line yields a FWHM of $\gtrsim 6 \text{ km s}^{-1}$ for MM-1 and MM-2. The linewidth is still significantly larger than the typical NH_3 linewidth of 2 km s^{-1} in the extended emission. The increase of linewidth in NH_3 and CH_3CN is consistent with the enhanced infall/rotation in the circumstellar material surrounding the star. However, due to the dominance of velocity shift between the MM-1 and MM-2 cores, no rotational motion toward the individual cores can be discerned over a scale of $> 1''$.

The study of the AFGL 5142 region highlights the complex kinematics in cluster forming regions where multiple massive stars compete for gravitational influence. In such an environment, extended rotating disks are likely truncated by the tidal interaction. The relative motion of dense cores surrounding massive stars can dominate the kinematics, and even create false signal of rotation. High angular resolution observations in continuum and spectral lines are the key in understanding the kinematics in these regions.

Despite the complexity in the core, the molecular outflows seen in CO and SO at larger scales provide insight in the formation process of stars in the cluster environment. By physical connection, the well collimated outflows indirectly suggest the presence of circumstellar accretion disks toward the three protostars in this cluster environment. One issue under debate in the past few years has been the formation mechanism of massive stars. In contrast to low-mass stars that stellar radiation exerts little dynamical influence on the infalling material, strong radiation from massive stars becomes a barrier to infall and may even prevent the formation of stars beyond $8 M_\odot$ (Larson 1969; Larson & Starrfield 1971; Kahn 1974; Yorke & Krügel 1977; Wolfire & Cassinelli 1987). Several solutions have been proposed to alleviate this radiation problem. The most effective solution is a flattened accretion disk (Nakano 1989; Jijina & Adams 1996; Yorke & Sonnhalter 2002) which shields most infalling material from the stellar radiation. An additional benefit of a flattened disk is that photons can escape through the lower density region along the polar axis of the disk (Yorke & Sonnhalter 2002; Krumholz et al. 2005). All the above mentioned solutions build upon the notion that massive stars form through gravitational collapse and disk accretion process (McKee & Tan 2002; Keto 2003). Bonnell et al. (1998) and Bonnell & Bate (2002) put forward an alternative process in which massive stars form through multiple mergers/collisions of low-mass protostars. This coalescence model appears to circumvent the radiation problem, but requires exceedingly high stellar density ($\gtrsim 10^6 \text{ stars pc}^{-3}$) in order for the process to be effective. In addition, the model still faces the radiation problem if the mechanical energy of the merging stars is released through radiation (Bally & Zinnecker 2005).

These two schools of models can be tested by observations (Zhang 2005; Cesaroni et al. 2006). Unlike the infall/accretion model, the coalescence scenario does not produce well collimated outflows from massive young stars (Bally & Zinnecker 2005). Our observations indicate that the coalescence model does not appear to be at work in this high-mass star formation region, since collimated outflows point to an alternative process: *i.e.* disk mediated accretion. At the same time, the coalescence model requires high stellar density ($\gtrsim 10^6 \text{ pc}^{-3}$) for merger to be effective. This stellar density requirement is not likely met in this region.

The coalescence scenario is a variation of the competitive accretion model (Bonnell & Bate 2002; Bonnell et al. 2004) in which a cluster of low-mass protostars with a common gravitational potential accretes the distributed gas from a reservoir of material in molecular cloud. Protostars located near the center of the potential accrete at a higher rate because of a stronger gravitational pull, and experience faster mass growth. This model explains the stellar initial mass function observed (Bonnell & Bate 2002; Bonnell et al. 2004). The main difference between the turbulent accretion and competitive accretion is that in the former model protostars accrete the gravitationally bound gas, whereas in the competitive accretion model massive protostars accrete mostly from the gravitationally unbound gas. As a consequence, the competitive accretion model predicts that the final mass of massive stars does not correlate with the core mass (Bonnell et al. 2004). In addition, the accretion rate in the turbulent accretion model goes with the turbulent velocity V_t as V_t^3/G , while in the competitive accretion model the accretion rate goes as $4\pi\rho\frac{(GM)^2}{V_t^3}$ for Bondi-Hoyle accretion. Here G is the gravitational constant, ρ the gas density, and M the mass of the accreting star. We estimate the accretion rate using the parameters derived here. For $V_t = 2.5 \text{ km s}^{-1}$, $M = 5 M_\odot$, and $\rho = 10^5 \text{ cm}^{-3}$ (the mean density in the core), we find an accretion rate of $4 \times 10^{-3} M_\odot \text{ yr}^{-1}$ for turbulent accretion, and $2 \times 10^{-6} M_\odot \text{ yr}^{-1}$ for Bondi-Hoyle accretion. The rate of $4 \times 10^{-3} M_\odot \text{ yr}^{-1}$ is sufficiently high to account for the mass loss in the outflow, whereas the rate of $2 \times 10^{-6} M_\odot \text{ yr}^{-1}$ appears to be too low to account for the mass loss rate in the outflow. On the other hand, the accretion rate is sensitive to turbulent velocity. The measured line width reported in Table 2 is probably affected by systematic motion (infall/rotation and outflow) in the core. If assuming a smaller value of $V_t = 1.5 \text{ km s}^{-1}$ based on the NH_3 line width in the extended core (Zhang et al. 2002), we find an accretion rate of $8 \times 10^{-4} M_\odot \text{ yr}^{-1}$ for turbulent accretion, and $1 \times 10^{-5} M_\odot \text{ yr}^{-1}$ for Bondi-Hoyle accretion. The latter value is still somewhat low, but closer to the accretion rate required for producing the observed outflows (Zhang et al. 2005). Although the test of the two models based on the AFGL 5142 data appears to be inclusive, it is hopeful that future observations of massive cores at earlier evolutionary stage will provide measurements of relevant physical parameters, especially turbulent velocity, and thus provide more definitive test of the two models.

5. Conclusion

High resolution ($1''$) observations with the SMA identified a high-mass protocluster in AFGL5142. The 1.3mm image reveals 5 continuum peaks with large variations in molecular line emission. Two mm cores, MM-1 and MM-2, are associated with the CH_3CN emission with rotational temperatures of ~ 90 and 250 K, and abundance of 1×10^{-8} and 4×10^{-8} , respectively. The higher temperature and inferred high luminosity indicate that they like form massive protostars. The remaining three cores do not have detectable CH_3CN and CH_3COH emission, and likely harbors less massive (or less evolved) protostars,

The CO and SO emission reveal at least three possible molecular outflows. The terminal velocity of the CO emission reaches up to 50 km s^{-1} . The outflows have masses of $3 M_\odot$, and momentum of $12\text{-}20 M_\odot \text{ km s}^{-1}$, typical of those associated with high-mass stars. Both CO and SiO emission in the dominant outflow A have terminal velocities increase with the distance from the star. The presence of multiple collimated outflows in this protocluster provide indirect evidence that accretion is the dominant process for the formation of the massive protostars in this cluster.

We thank P. Caselli for insightful discussions. H.B. acknowledges financial support by the Emmy-Noether-Programm of the Deutsche Forschungsgemeinschaft (DFG, grant BE2578).

REFERENCES

- Anglada, G., Villuendas, E., Estalella, R., et al. 1998, *AJ*, 116, 2953
- Bachiller, R., Pérez Gutiérrez, M., Kumar, M. S. N., & Tafalla, M. 2001, *A&A*, 372, 899
- Bally, J. & Zinnecker, H. 2005, *AJ*, 129, 2281
- Beuther, H., Zhang, Q., Greenhill, L. J., et al. 2004a, *ApJ*, 616, L31
- Beuther, H., Zhang, Q., Hunter, T. R., et al. 2004b, *ApJ*, 616, L19
- Bonnell, I. A. & Bate, M. R. 2002, *MNRAS*, 336, 659
- Bonnell, I. A., Bate, M. R., & Zinnecker, H. 1998, *MNRAS*, 298, 93
- Bonnell, I. A., Vine, S. G., & Bate, M. R. 2004, *MNRAS*, 349, 735

- Ceccarelli, C., Loinard, L., Castets, A., Tielens, A. G. G. M., & Caux, E. 2000, *A&A*, 357, L9
- Cesaroni, R., Felli, M., Jenness, T., et al. 1999, *A&A*, 345, 949
- Cesaroni, R., Galli, D., Lodato, G., Walmsley, C. M., & Zhang, Q. 2006, *ArXiv Astrophysics e-prints*
- Chandler, C. J., Brogan, C. L., Shirley, Y. L., & Loinard, L. 2005, *ApJ*, 632, 371
- Chen, H.-R., Welch, W. J., Wilner, D. J., & Sutton, E. C. 2006, *ApJ*, 639, 975
- Chen, Y., Yao, Y., Yang, J., Zeng, Q., & Sato, S. 2005, *ApJ*, 629, 288
- Choi, M., Evans, N. J., & Jaffe, D. T. 1993, *ApJ*, 417, 624
- Curiel, S., Rodriguez, L. F., Bohigas, J., et al. 1989, *Astrophysical Letters Communications*, 27, 299
- Elitzur, M., Hollenbach, D. J., & McKee, C. F. 1989, *ApJ*, 346, 983
- Estalella, R., Mauersberger, R., Torrelles, J. M., et al. 1993, *ApJ*, 419, 698
- Felli, M., Palagi, F., & Tofani, G. 1992, *A&A*, 255, 293
- Goddi, C., Moscadelli, L., Alef, W., et al. 2005, *A&A*, 432, 161
- Gueth, F. & Guilloteau, S. 1999, *A&A*, 343, 571
- Herbst, E. & Leung, C. M. 1990, *A&A*, 233, 177
- Hildebrand, R. H. 1983, *QJRAS*, 24, 267
- Hillenbrand, L. A. 1997, *AJ*, 113, 1733
- Hillenbrand, L. A. & Hartmann, L. W. 1998, *ApJ*, 492, 540
- Ho, P. T. P., Moran, J. M., & Lo, K. Y. 2004, *ApJ*, 616, L1
- Hunter, T. R., Testi, L., Taylor, G. B., et al. 1995, *A&A*, 302, 249
- Hunter, T. R., Testi, L., Zhang, Q., & Sridharan, T. K. 1999, *AJ*, 118, 477
- Jijina, J. & Adams, F. C. 1996, *ApJ*, 462, 874
- Kahn, F. D. 1974, *A&A*, 37, 149

- Keto, E. 2003, *ApJ*, 599, 1196
- Krumholz, M. R., McKee, C. F., & Klein, R. I. 2005, *Nature*, 438, 332
- Kuan, Y.-J., Huang, H.-C., Charnley, S. B., et al. 2004, *ApJ*, 616, L27
- Lada, C. J. & Fich, M. 1996, *ApJ*, 459, 638
- Larson, R. B. 1969, *MNRAS*, 145, 271
- Larson, R. B. & Starrfield, S. 1971, *A&A*, 13, 190
- Lebrón, M., Beuther, H., Schilke, P., & Stanke, T. 2006, *A&A*, 448, 1037
- McKee, C. F. & Tan, J. C. 2002, *Nature*, 416, 59
- Nakano, T. 1989, *ApJ*, 345, 464
- Pestalozzi, M. R., Minier, V., & Booth, R. S. 2005, *A&A*, 432, 737
- Scoville, N. Z. & Kwan, J. 1976, *ApJ*, 206, 718
- Shepherd, D. S., Yu, K. C., Bally, J., & Testi, L. 2000, *ApJ*, 535, 833
- Slysh, V. I., Dzura, A. M., Val'tts, I. E., & Gerard, E. 1997, *A&AS*, 124, 85
- Snell, R. L., Huang, Y.-L., Dickman, R. L., & Claussen, M. J. 1988, *ApJ*, 325, 853
- Su, Y., Zhang, Q., & Lim, J. 2004, *ApJ*, 604, 258
- Swade, D. A. 1989, *ApJ*, 345, 828
- Torrelles, J. M., Gómez, J. F., Anglada, G., et al. 1992, *ApJ*, 392, 616
- Viti, S., Girart, J. M., Garrod, R., Williams, D. A., & Estalella, R. 2003, *A&A*, 399, 187
- Viti, S. & Williams, D. A. 1999, *MNRAS*, 310, 517
- Wilner, D. J., Wright, M. C. H., & Plambeck, R. L. 1994, *ApJ*, 422, 642
- Wolfire, M. G. & Cassinelli, J. P. 1987, *ApJ*, 319, 850
- Yorke, H. W. & Krügel, E. 1977, *A&A*, 54, 183
- Yorke, H. W. & Sonnhalter, C. 2002, *ApJ*, 569, 846

- Zhang, Q. 2005, in IAU Symposium, ed. R. Cesaroni, M. Felli, E. Churchwell, & M. Walm-
sley, 135–144
- Zhang, Q., Ho, P. T. P., & Ohashi, N. 1998, ApJ, 494, 636
- Zhang, Q., Ho, P. T. P., & Wright, M. C. H. 2000, AJ, 119, 1345
- Zhang, Q., Ho, P. T. P., Wright, M. C. H., & Wilner, D. J. 1995, ApJ, 451, L71+
- Zhang, Q., Hunter, T. R., Brand, J., et al. 2005, ApJ, 625, 864
- Zhang, Q., Hunter, T. R., Sridharan, T. K., & Ho, P. T. P. 2002, ApJ, 566, 982

Table 1: Parameters of Continuum Sources^a

Name	R.A. ^a (J2000)	Dec. ^a (J2000)	S_{peak}	Mass ^b
	(<i>h m s</i>)	(<i>° ' "</i>)	mJy/beam	M_{\odot}
CM-1A	05 30 48.014	33 47 54.66	0.65	-
CM-1B	05 30 48.025	33 47 54.41	0.64	-
CM-2	05 30 47.999	33 47 52.57	0.35	-
MM-1	05 30 48.037	33 47 54.55	240	3
MM-2	05 30 48.034	33 47 53.72	230	3
MM-3	05 30 47.979	33 47 52.42	84	2
MM-4	05 30 48.193	33 47 54.62	35	0.9
MM-5	05 30 47.849	33 47 52.20	27	0.8

^aThere appears to be an offset of $0''.2$ between the 225GHz data, and the 8.4 GHz data and NH_3 data from the VLA. This offset is within the calibration error in the 225GHz dataset. Minor mm peaks less than 6σ are not reported here.

^bWe assume dust temperature of 45 K for MM-1 and MM-2 based on the estimate in Hunter et al. (1999), and 20 K for MM-3, MM-4 and MM-5 based on the NH_3 observations (Zhang et al. 2002)

Table 2: Lines Detected in the Hot Core^a

Frequency GHz	Line	E_{upper} K	MM-1		MM-2	
			S K	FWHM km s ⁻¹	S K	FWHM km s ⁻¹
219.560	C ¹⁸ O 2-1	16	9.4	2.9	11.7	4.4
219.733	HNCO 10 _{2,9} - 9 _{2,8}	230	4.5	-	8.0	4.8
219.737	HNCO 10 _{2,8} - 9 _{2,7}	230	4.5	-	8.0	4.8
219.798	HNCO 10 _{0,10} - 9 _{0,9}	59	4.8	5.8	12.4	4.9
219.909	H ₂ ¹³ CO 3 _{1,2} - 2 _{1,1}	23	3.4	3.7	5.4	3.7
219.949	SO 6 ₅ - 5 ₄	35	20.2	5.6	30.0	5.8
220.079	CH ₃ OH 8 _{0,8} - 7 _{1,6}	96	14.2	4.9	25.3	3.6
220.399	¹³ CO 2-1	16	24.0	2.2	20.4	5.8
220.584	HNCO 10 _{1,9} - 9 _{1,8}	59	-	-	11.4	4.9
220.594	CH ₃ CN 12 ₆ - 11 ₆	326	4.7	4.7	13.1	4.0
220.641	CH ₃ CN 12 ₅ - 11 ₅	248	4.6	4.7	10.7	4.0
220.679	CH ₃ CN 12 ₄ - 11 ₄	184	5.4	4.7	16.3	4.0
220.709	CH ₃ CN 12 ₃ - 11 ₃	134	14.6	4.7	17.2	4.0
220.730	CH ₃ CN 12 ₂ - 11 ₂	98	10.3	4.7	20.1	4.0
220.743	CH ₃ CN 12 ₁ - 11 ₁	76	10.0	4.7	22.3	4.0
220.747	CH ₃ CN 12 ₀ - 11 ₀	69	12.3	4.7	24.1	4.0
229.589	CH ₃ OH 15 _{4,11} - 16 _{3,13} E	374	4.2	5.3	10.0	6.0
229.759	CH ₃ OH 8 _{-1,8} - 7 _{0,7} E	89	12.3	6.3	22.7	4.4
229.864	CH ₃ OH 19 _{5,15} - 20 _{4,16} A+	579	3.4	-	6.0	6.0
230.027	CH ₃ OH 3 _{-2,2} - 4 _{-1,4} E	39	6.0	5.8	15.8	4.0
230.538	¹² CO 2-1 ^b	17	40.0	8.6	40.0	8.6
231.061	OCS 19-18	111	7.2	5.8	7.3	7.5

^aWe listed lines detected above 5 σ level.

^bThe CO 2-1 spectrum is self-absorbed. The Gaussian fitting is uncertain.

Table 3: Outflow Parameters^a

Outflow	PA(°)	V_{Max}^b km s ⁻¹	T_{dyn}^c 10 ⁴ yrs	Mass M _⊙	Momentum M _⊙ km s ⁻¹	Energy 10 ⁴⁵ ergs
A	5	50	0.5	2.5	12	1.1
B	35	25	1	3.0	20	2.0
C	-60	25	1	3.0	20	2.0

^aParameters are not corrected for orientation of the outflow.

^bThe terminal velocity detectable at an rms of 0.09 Jy

^cDynamic timescale computed from l/V_{Max} , with l the length of the outflow and V_{Max} the terminal velocity of the outflow.

Figure Captions

Figure 1: 225 GHz (1.3mm) and 8.4 GHz (3.6cm) continuum emission toward AFGL 5142. The 1.3 mm continuum peaks (MM-1, MM-2, MM-3, MM-4 and MM-5) are marked by stars on both panels. The 3.6 cm continuum peaks (CM-1A, CM-1B and CM-2) are marked by filled squares on the right panel. The H₂O maser positions from Hunter et al. (1999) are marked by crosses. The contour levels are in steps of 12 mJy/beam for the 225GHz image, and 0.2 mJy/beam for the 8.4 GHz image. The synthesized beam is denoted at the lower-left corner of each panel.

Figure 2: Line spectra toward MM-1, MM-2, MM-3 and the red-shifted peak in outflow A (the filled triangle in Figure 3) for the lower side band (LSB) and upper sideband (USB). The spectra for the mm continuum sources are from images with a resolution of $1''.3 \times 0''.8$ (The conversion factor from Jy/beam to Kelvin is 17 K/Jy). The spectrum for the outflow position is made with Natural weighting and tapering of visibilities, resulting in an angular resolution of $4''.0 \times 3''.3$ (The conversion factor from Jy/beam to Kelvin is 1.9 K/Jy).

Figure 3: Images of the velocity integrated flux of ¹³CO J=2-1, C¹⁸O J=2-1, SO 6₅ – 5₄, CH₃OH 8_{-1,8} – 7_{0,7} E, OCS J=19-18, and HNC O 10_{0,10} – 9_{0,9} for AFGL 5142. The range of the integration covers the entire velocity of the line. The stars mark the position of the mm continuum peaks MM-1, MM-2 and MM-3, MM-4 and MM-5. The triangle in the SO panel marks the position of the spectrum from the outflow A shown in Figure 2. The contour levels are in steps of 3 Jy km s⁻¹ beam⁻¹ starting from 3 Jy km s⁻¹ beam⁻¹, 2 Jy km s⁻¹ beam⁻¹ starting from 2 Jy km s⁻¹ beam⁻¹ for SO 6₅ – 5₄, and C¹⁸O J=2-1 lines, and in steps of 1 Jy km s⁻¹ beam⁻¹ starting from 1 Jy km s⁻¹ beam⁻¹ for CH₃OH 8_{-1,8} – 7_{0,7} E, OCS J=19-18 lines, and HNC O 10_{0,10} – 9_{0,9} lines. The size of the primary beam (57'') is marked by the dashed circle in the upper-left panel. The synthesized beam is denoted by the shaded ellipse at the lower-left corner of each panel.

Figure 4: 4a: The integrated emission of the CH₃CN J=12-11. The contour levels are in steps of 2 Jy km s⁻¹ beam⁻¹. The stars mark the position of the mm continuum peaks MM-1, MM-2, MM-3, MM-4 and MM-5. The synthesized beam is denoted by the shaded ellipse at the lower-left corner. 4b: The observed (thin lines) and model (thick lines) spectra toward the position of MM-1 and MM-2.

Figure 5: ¹²CO 2-1 emission toward AFGL 5142. The stars mark the position of the mm continuum peaks MM-1, MM-2, MM-3, MM-4 and MM-5. The plus symbols denote the near infrared H₂ emission knots (Hunter et al. 1999). Arrows mark the three molecular outflows A, B and C. The corresponding velocity range of the ¹²CO emission is labeled at the upper-right corner of each panel. The synthesized beam is denoted by the shaded ellipse

at the lower-left corner of the first panel. 5a: High velocity ^{12}CO 2-1 emission from the SMA data alone. The contour levels are in steps of 0.3 mJy/beam. 5b: Low velocity ^{12}CO 2-1 emission from combined SMA and CSO data. The contour levels are in steps of 0.6 mJy/beam.

Figure 6: The position velocity diagram of the ^{12}CO 2-1 emission. The CO data are from SMA alone. The cut is along the axis of outflows A, B and C, with position offset at MM-2. The contour levels are in steps of 0.4 Jy/beam. The vertical dashed lines mark the cloud systemic velocity of -3.9 km s^{-1} .

Figure 7: Channel maps of the SO $6_5 - 5_4$ line. The contour levels are in steps of 0.4 Jy/beam. The stars mark the position of the mm continuum peaks MM-1, MM-2, MM-3, MM-4 and MM-5. The plus symbols denote the near infrared H_2 emission knots (Hunter et al. 1999). Arrows mark the three molecular outflows A, B and C. The synthesized beam is denoted by the shaded ellipse at the lower-left corner of the first panel.

Figure 8: Channel maps of the CH_3OH $8_{-1,8} - 7_{0,7}$ E line. The contour levels are in steps of 0.4 Jy/beam. The stars mark the position of the mm continuum peaks MM-1, MM-2, MM-3, MM-4 and MM-5. The plus symbols denote the near infrared H_2 emission knots (Hunter et al. 1999). Arrows mark the three molecular outflows A, B and C. The synthesized beam is denoted by the shaded ellipse at the lower-left corner of the first panel.

Figure 9: The SiO 2-1 emission from Hunter et al. (1999) in contours overlaid on the ^{12}CO 2-1 emission in greyscale for outflow A. The cut of the position velocity plot is along the outflow axis with position offset from MM-2. The SiO emission is plotted in steps of 18 mJy beam $^{-1}$.

Figure 10: The ratios of the NH_3 (J,K)=(3,3) over (1,1), and NH_3 (J,K)=(4,4) over (1,1) emission (color) overlaid on the integrated emission of the NH_3 (J,K)=(1,1) line (contours). The images are taken from Zhang et al. (2002). The higher ratios denote higher temperatures. Arrows mark the three molecular outflows A, B and C. The stars mark the position of the mm continuum peaks MM-1, MM-2, MM-3, MM-4 and MM-5.

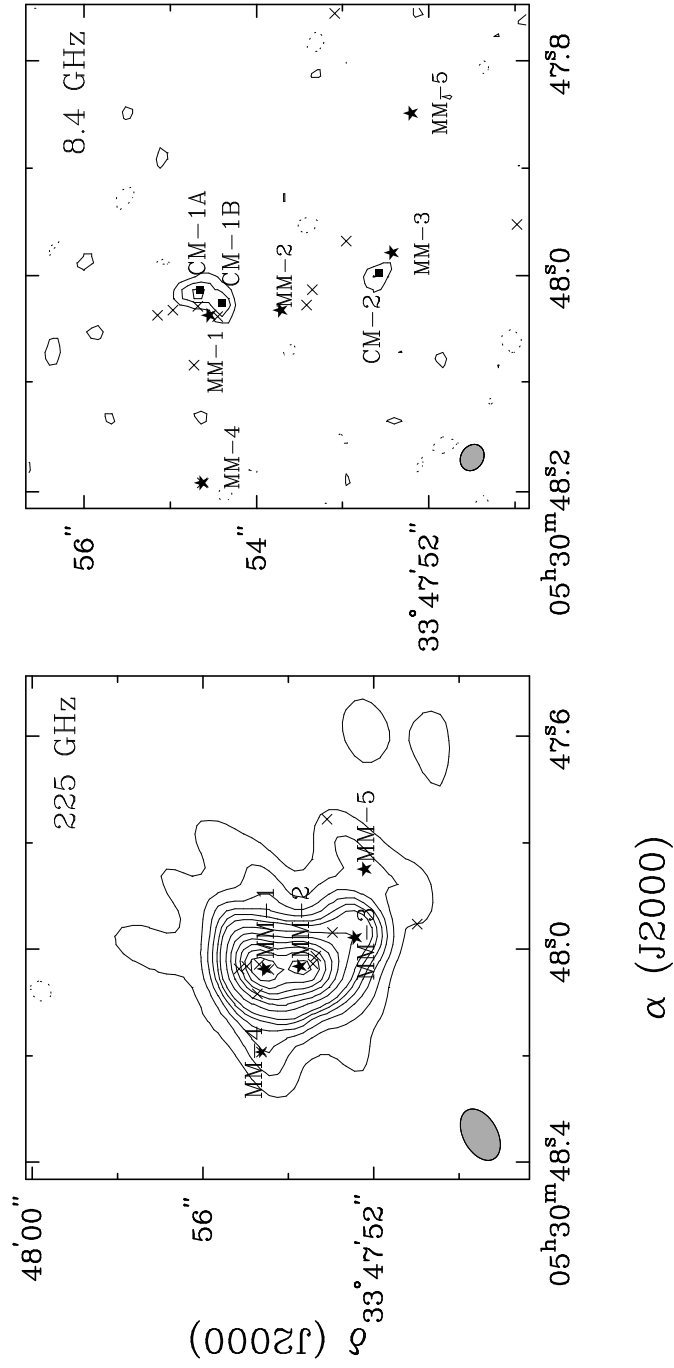


Fig. 1.—

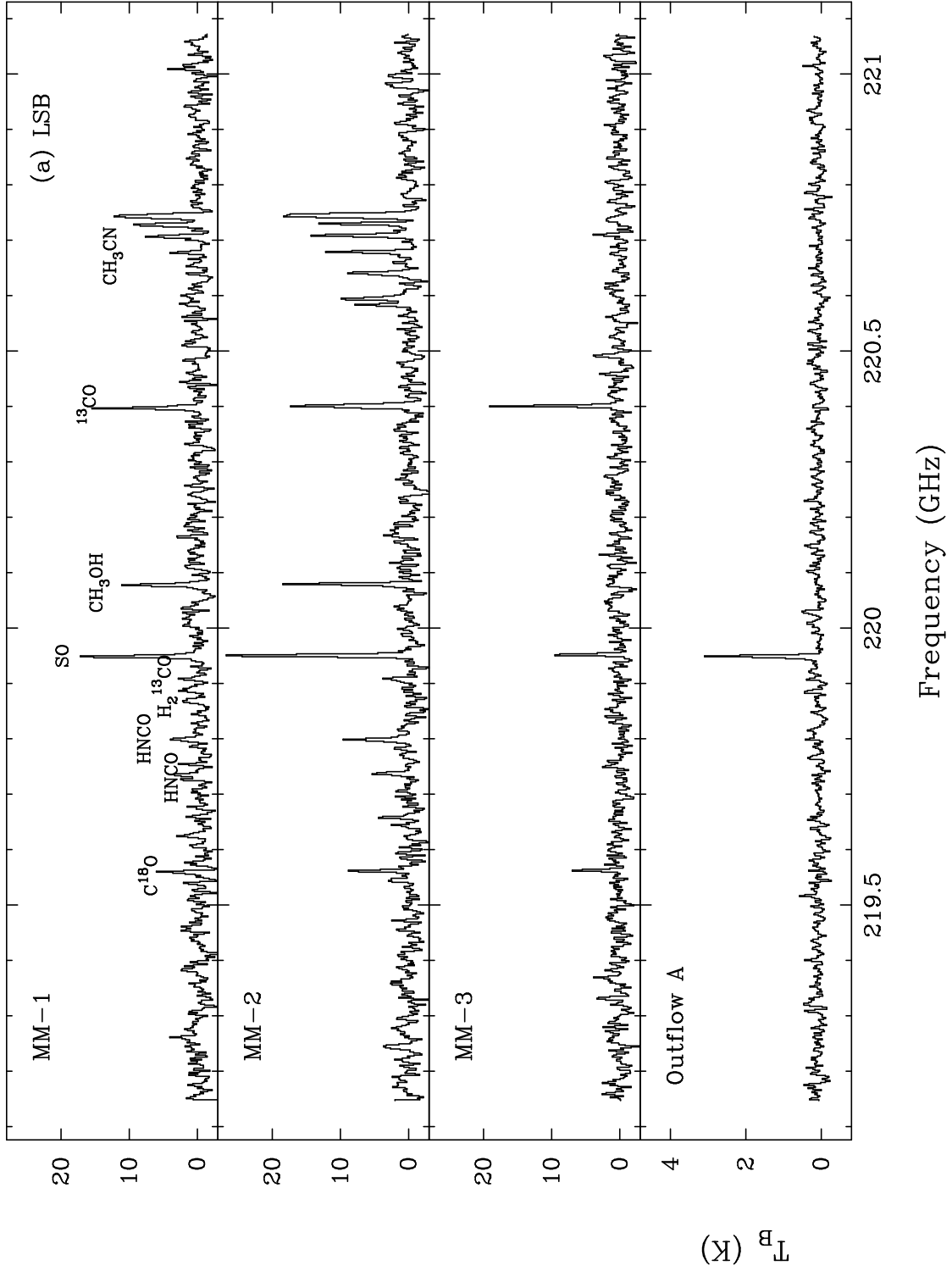


Fig. 2a.—

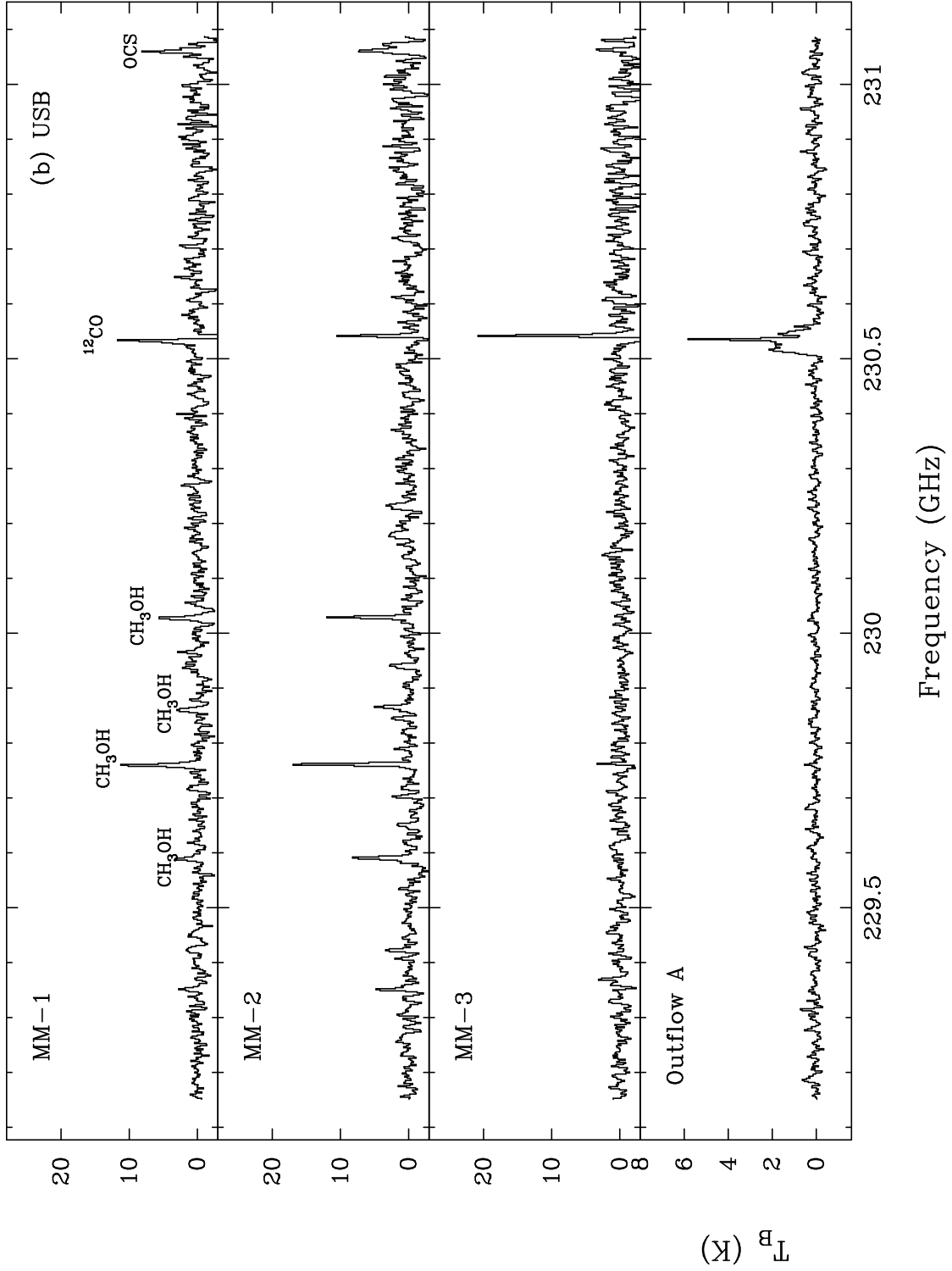


Fig. 2b.—

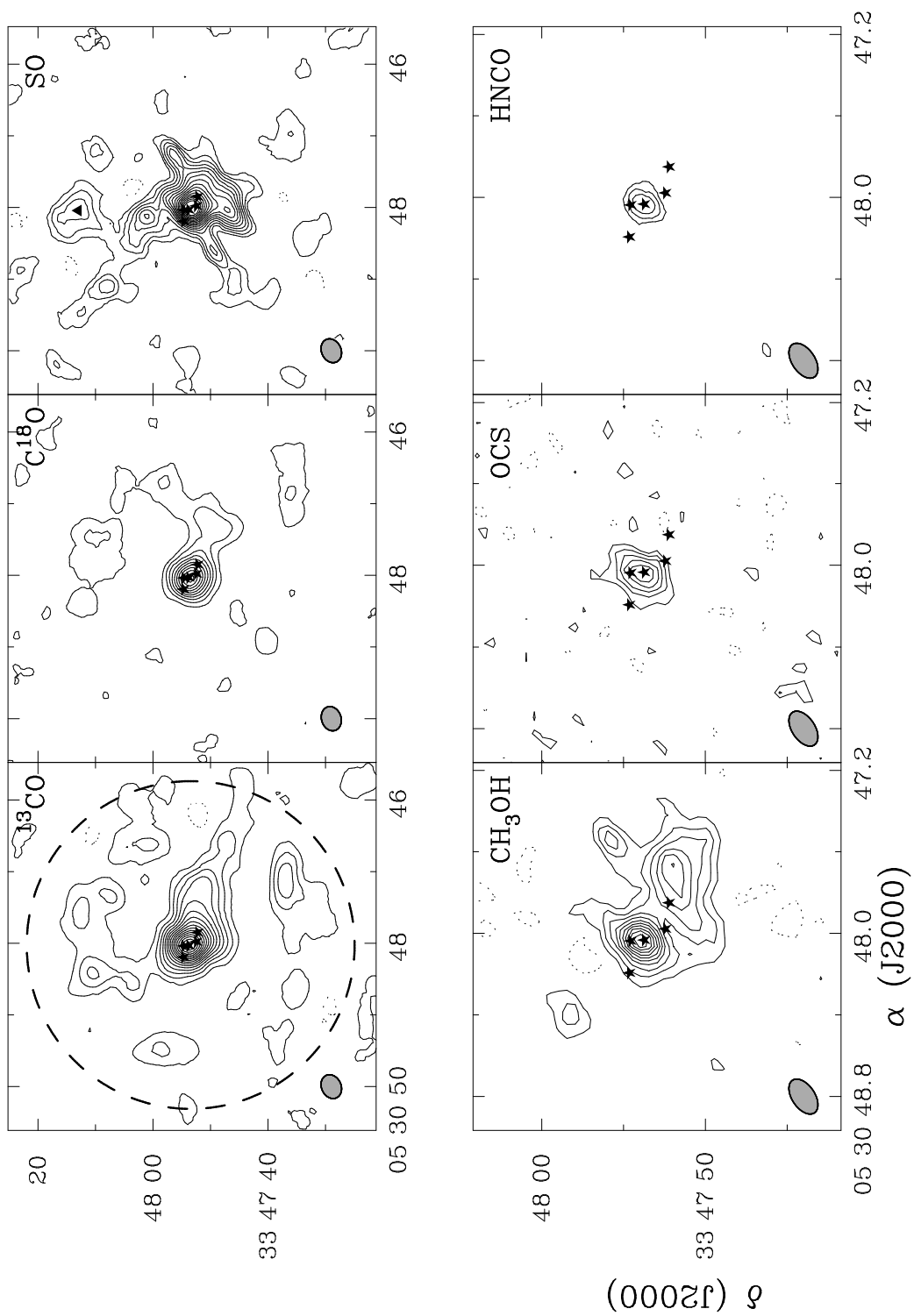


Fig. 3.—

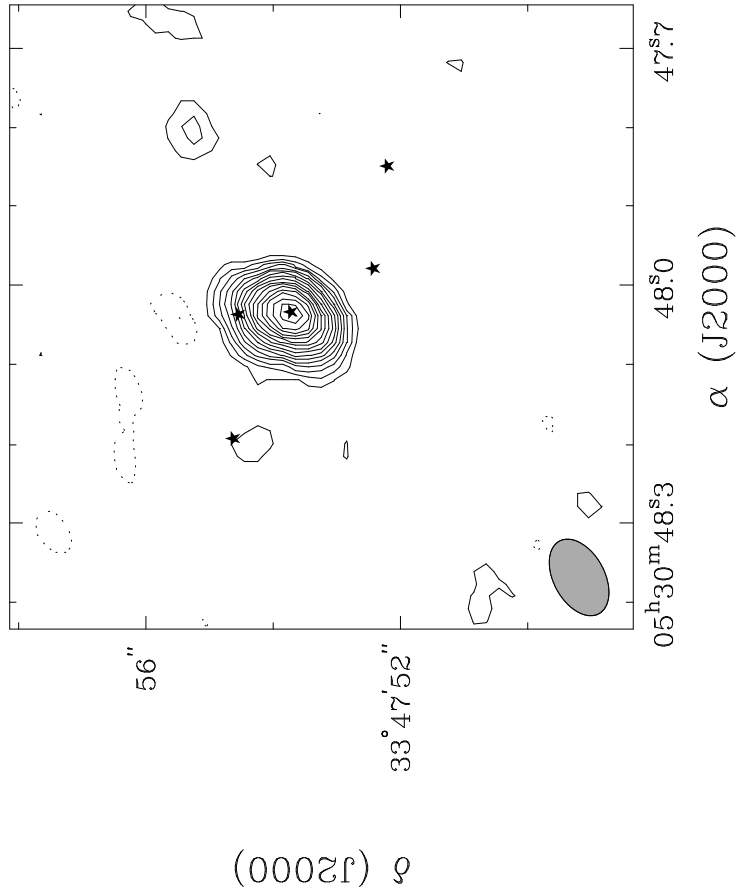


Fig. 4a.—

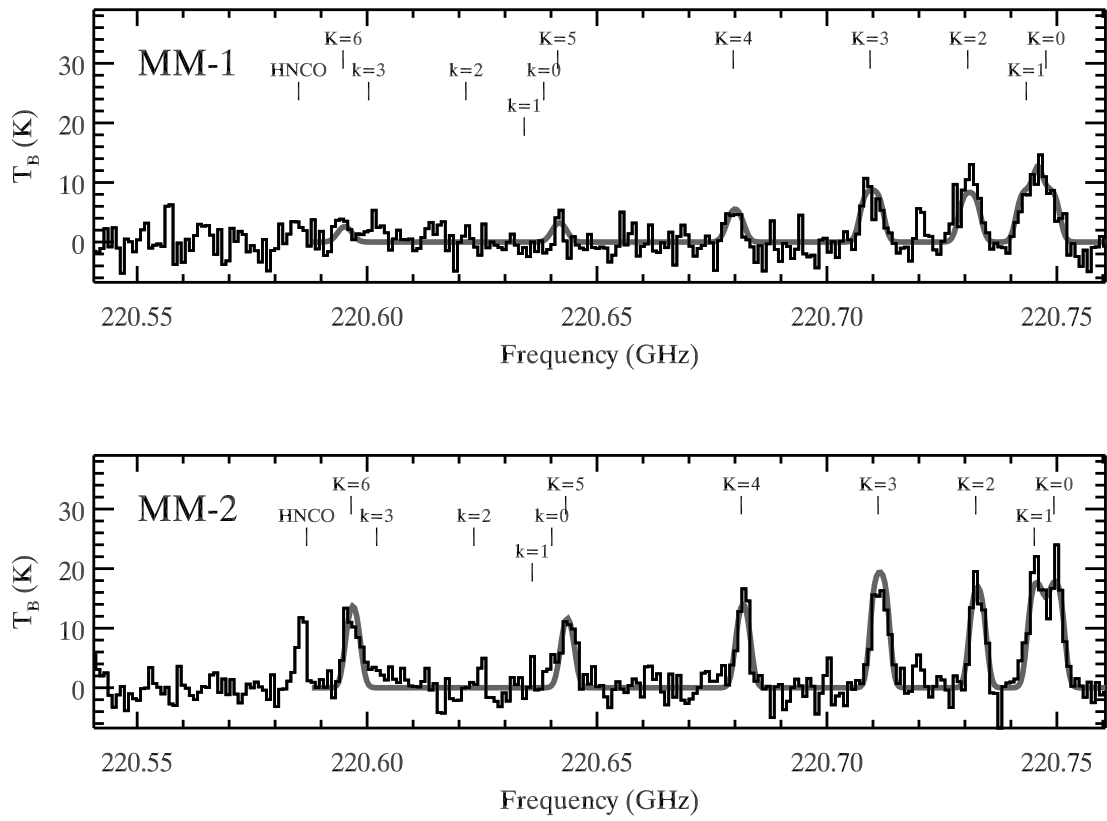


Fig. 4b.—

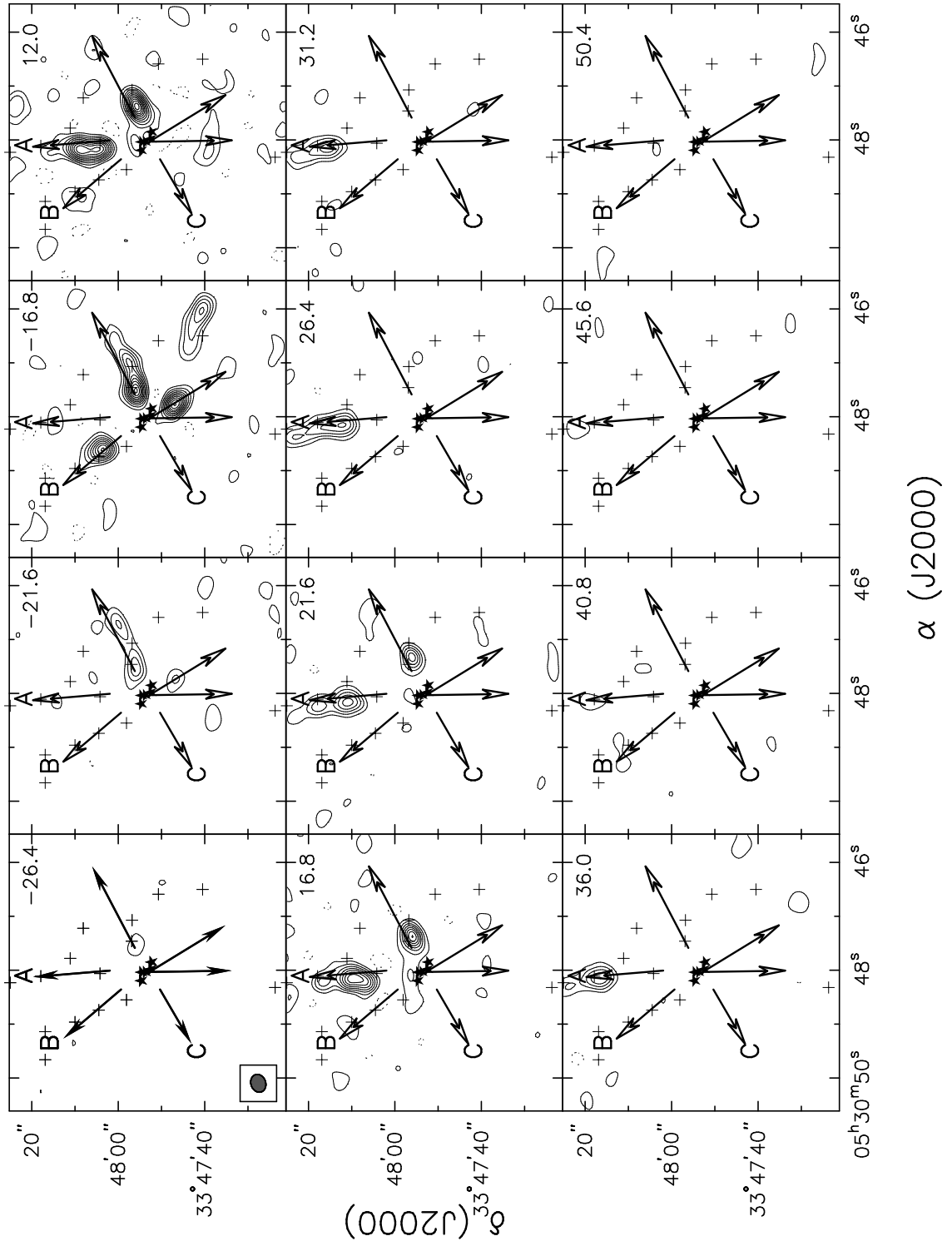


Fig. 5a.—

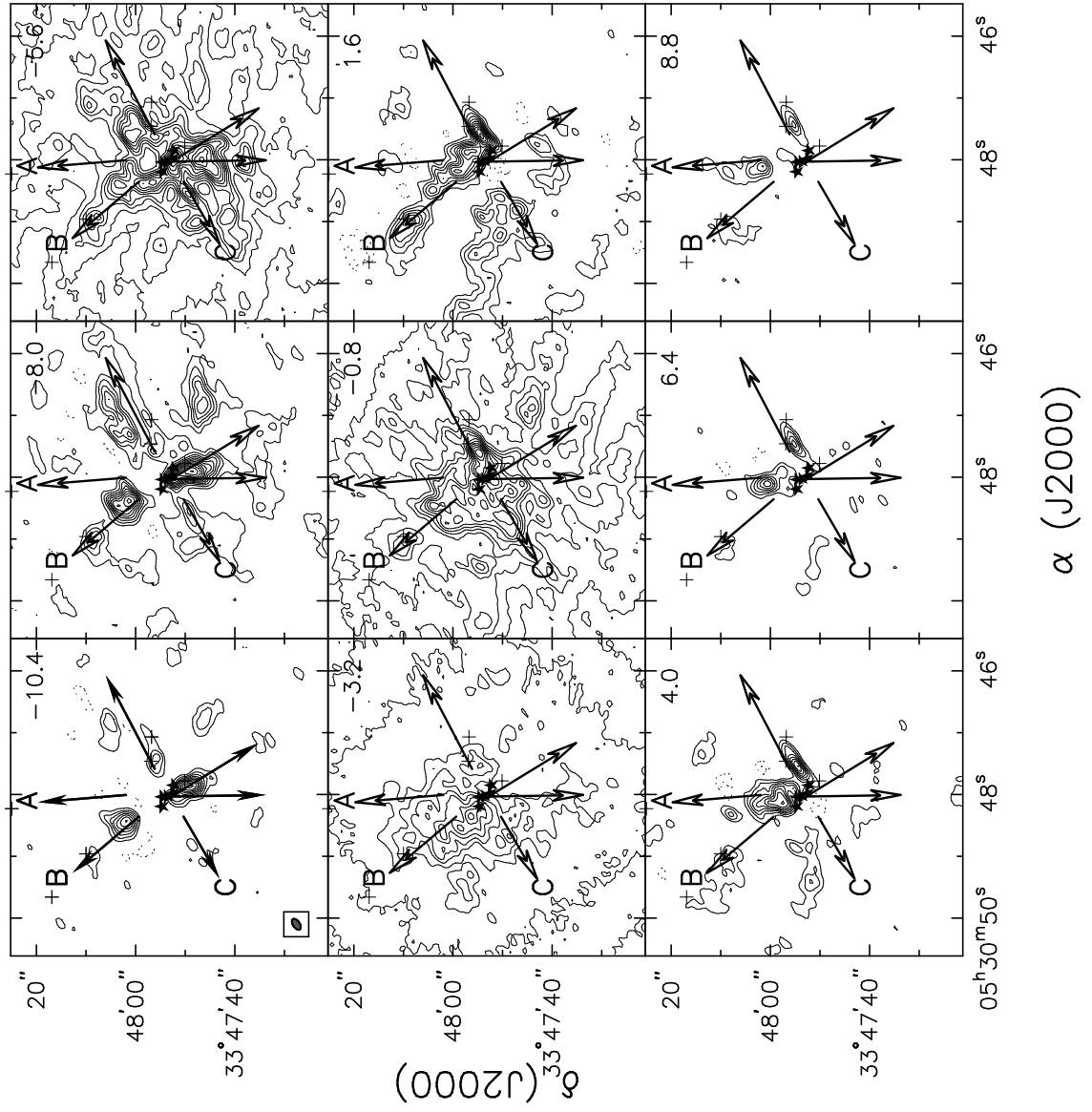


Fig. 5b.—

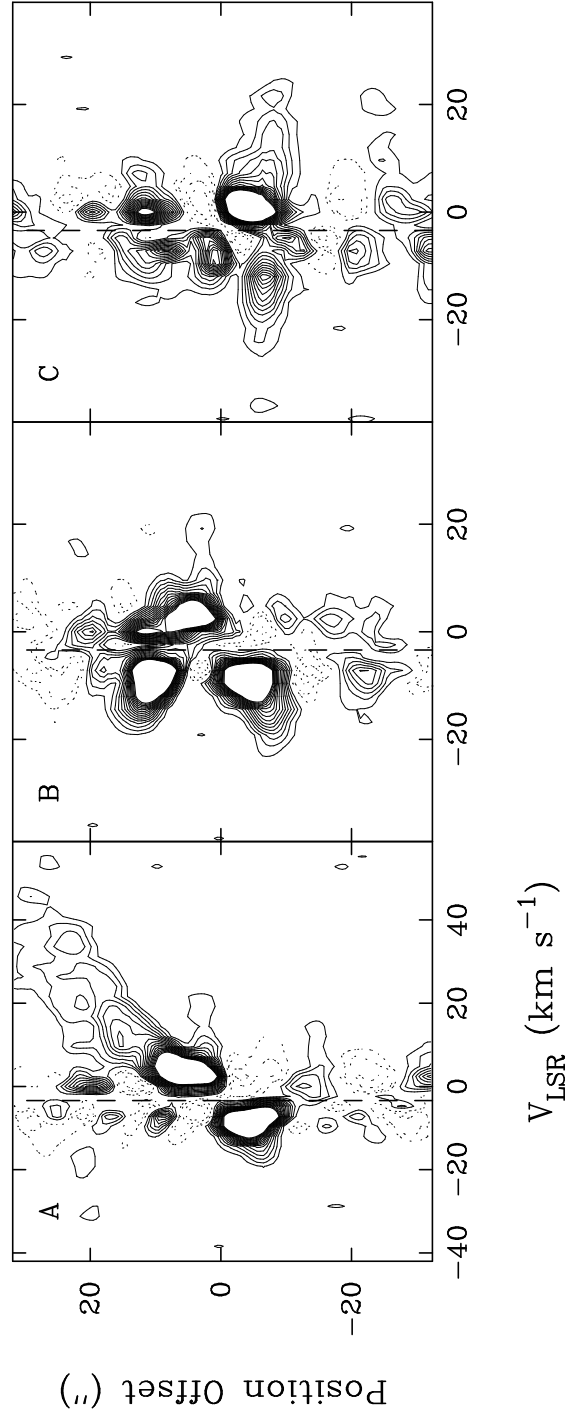


Fig. 6.—

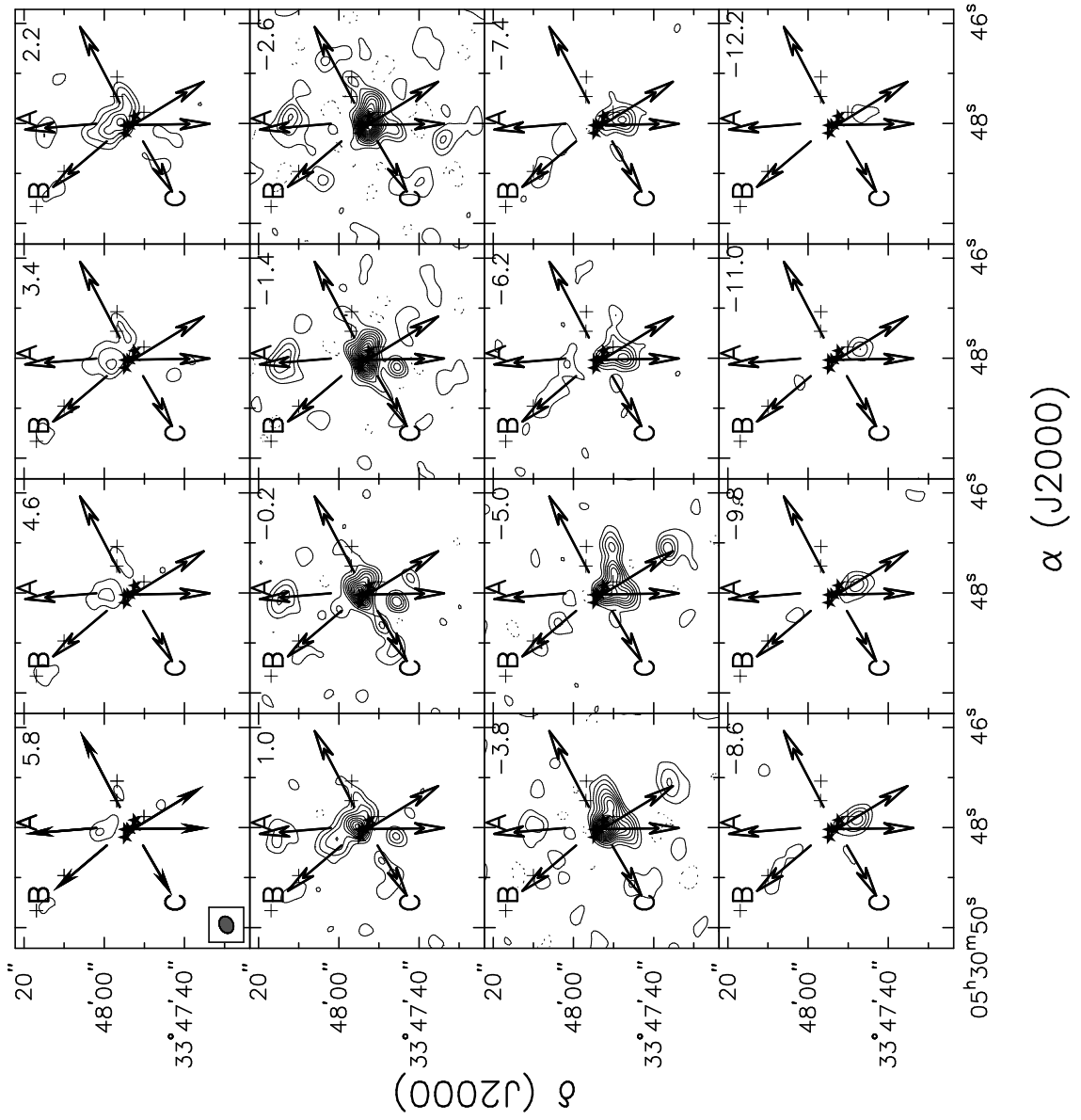


Fig. 7.—

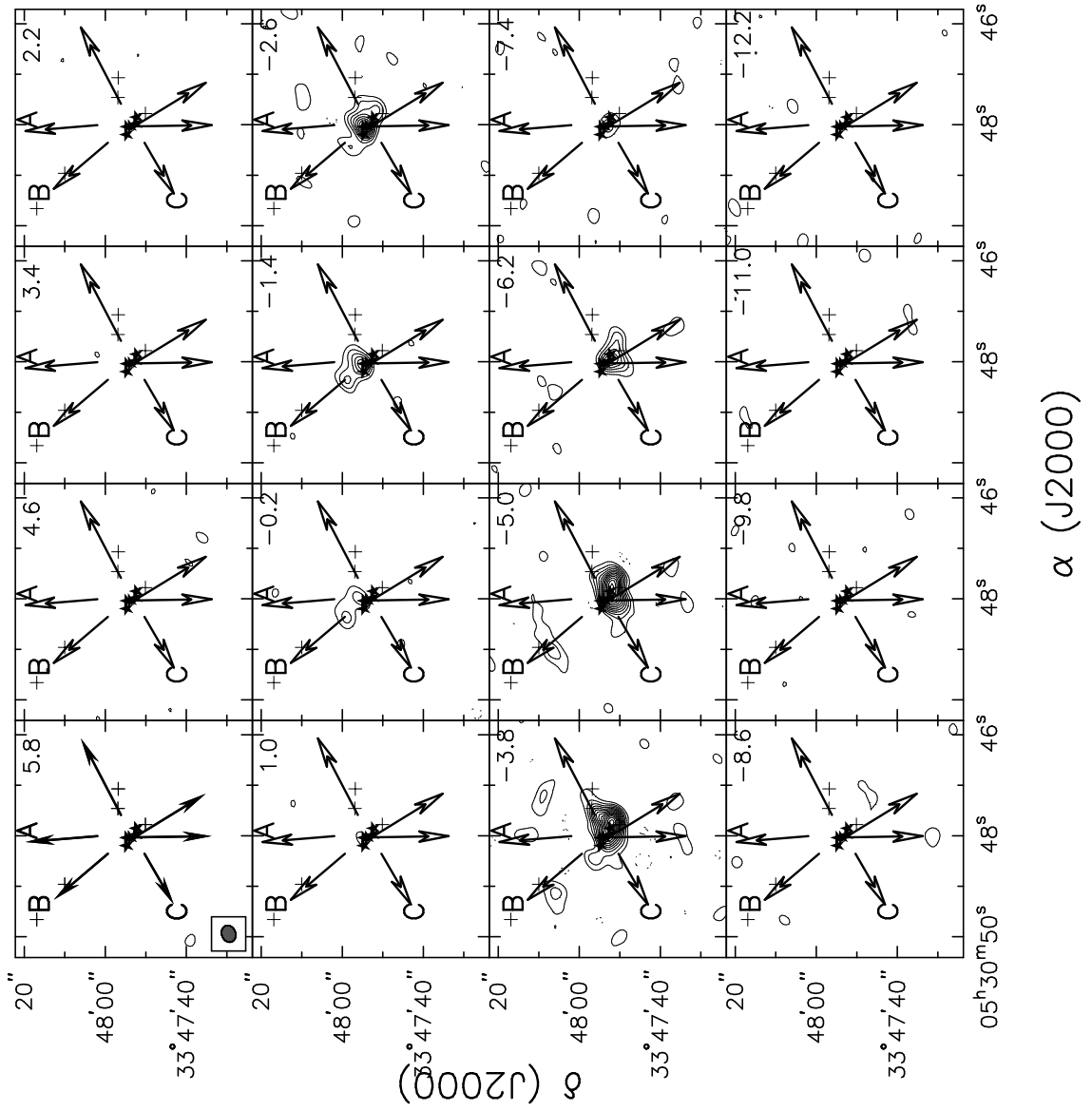


Fig. 8.—

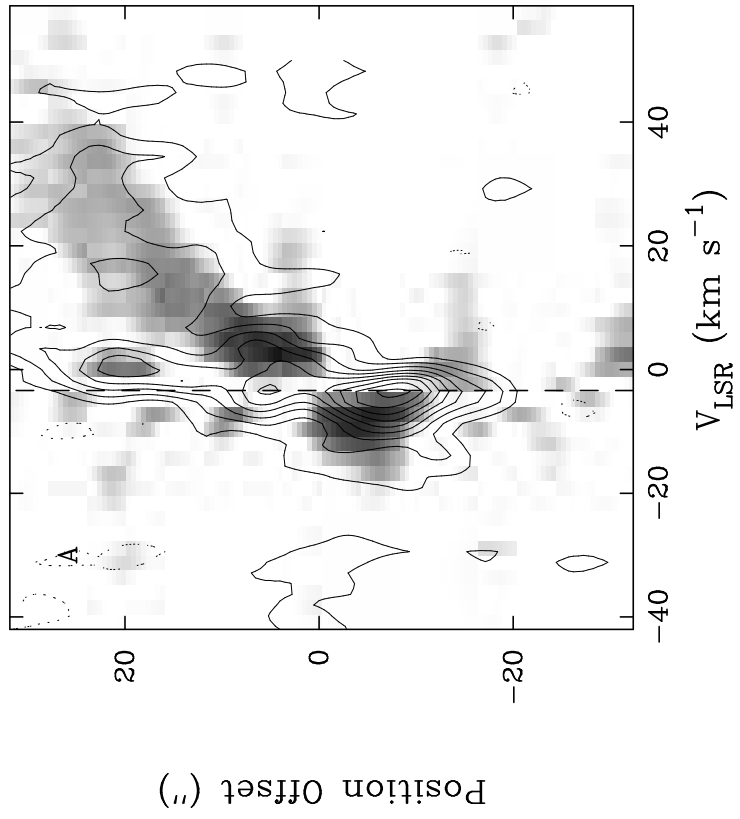


Fig. 9.—

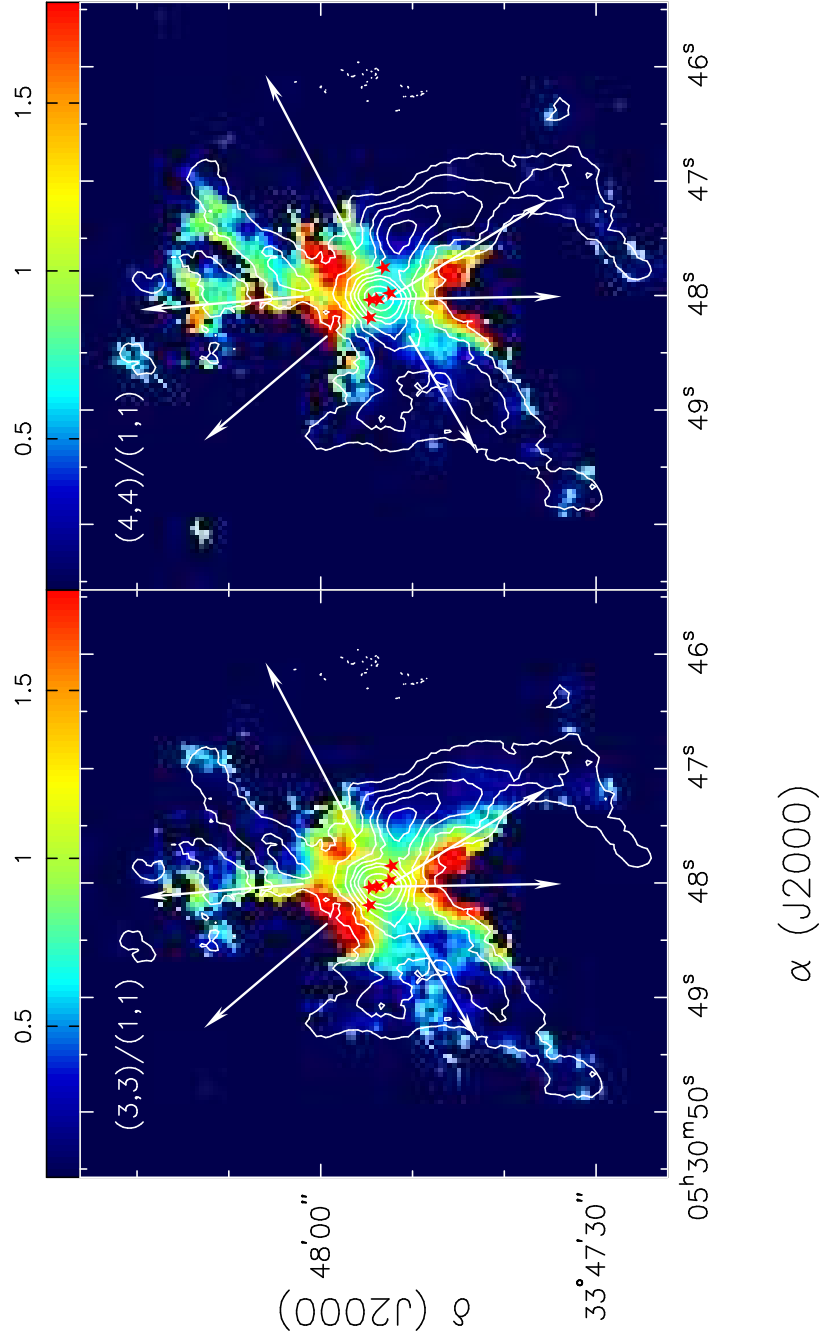


Fig. 10.—